



HAL
open science

Influence of pH on the interlayer cationic composition and hydration state of Ca-montmorillonite: analytical chemistry, chemical modelling and XRD profile modelling study.

Eric Ferrage, Christophe Tournassat, Emmanuel Rinnert, Bruno Lanson

► To cite this version:

Eric Ferrage, Christophe Tournassat, Emmanuel Rinnert, Bruno Lanson. Influence of pH on the interlayer cationic composition and hydration state of Ca-montmorillonite: analytical chemistry, chemical modelling and XRD profile modelling study.. *Geochimica et Cosmochimica Acta*, 2005, 69, pp.2797-2812. 10.1016/j.gca.2004.12.008 . hal-00106998

HAL Id: hal-00106998

<https://hal.science/hal-00106998v1>

Submitted on 17 Oct 2006

HAL is a multi-disciplinary open access archive for the deposit and dissemination of scientific research documents, whether they are published or not. The documents may come from teaching and research institutions in France or abroad, or from public or private research centers.

L'archive ouverte pluridisciplinaire **HAL**, est destinée au dépôt et à la diffusion de documents scientifiques de niveau recherche, publiés ou non, émanant des établissements d'enseignement et de recherche français ou étrangers, des laboratoires publics ou privés.

Influence of pH on the interlayer cationic composition and hydration state of Ca-montmorillonite: analytical chemistry, chemical modelling and XRD profile modelling study

Revised Version n°2

ERIC FERRAGE,^{1,2,*} CHRISTOPHE TOURNASSAT,^{2,3} EMMANUEL RINNERT^{2,4}
and BRUNO LANSON¹

¹ Environmental Geochemistry Group, LGIT, University of Grenoble-I P.O. Box 53, 38041 Grenoble, France.

² ANDRA, Parc de la Croix Blanche, 1/7 rue Jean Monnet, 92298 Châtenay-Malabry Cedex, France

³ BRGM, 3 avenue Claude Guillemin, 45060 Orléans Cedex 2, France

⁴ Laboratoire de Chimie Physique et Microbiologie pour l'Environnement, UMR 7564 CNRS- Université Henri Poincaré, 405 rue de Vandoeuvre, 54600 Villers-Lès-Nancy, France

* Corresponding author:

Eric Ferrage

Fax: +33 (0)4 7682 8101;

Tel: +33 (0)4 7682 8018;

E-mail: eric.ferrage@obs.ujf-grenoble.fr;

Keywords : smectite, hydration state, XRD modelling, pH, chemical modelling, interlayer protons

ABSTRACT

The hydration state of a <2 μm fraction of Ca-saturated SWy-2 montmorillonite was characterised after rapid equilibration (3 hours) under pH-controlled conditions (0.1-12.6 pH range). The solution composition was monitored together with the interlayer composition and X-ray diffraction (XRD) patterns were recorded on oriented preparations. Experimental XRD patterns were then fitted using a trial-and-error procedure to quantify the relative proportions of layers with different hydration states.

The montmorillonite is mostly bi-hydrated in basic and near-neutral conditions whereas it is mostly mono-hydrated at low pH. The transition from the bi-hydrated to the mono-hydrated state occurs through very heterogeneous structures. However, the proportion of the different layer types determined from XRD profile modelling and that derived from chemical modelling using Phreeqc2 code strictly coincide. This correlation shows that the hydration modification is induced by a H_3O^+ -for- Ca^{2+} exchange at low pH, the two species being distributed in different interlayers. This layer-by-layer exchange process occurs randomly in the layer stack.

Under alkaline conditions, results from XRD profile modelling and from near infrared diffuse reflectance spectroscopy (NIR-DRS) clearly demonstrate that there is no CaOH^+ -for- Ca^{2+} exchange at high pH. The apparent increase in Ca sorption in smectite interlayers with increasing pH is thus probably related to the precipitation of Calcium-Silicate-Hydrate (CSH) phases, which also accounts for the decrease in Si concentration under high-pH conditions. This precipitation is thermodynamically favoured.

1. INTRODUCTION

One of the possible multi-barrier storage concepts developed in France for intermediate-level long-lived radioactive wastes (ILLW wastes) consists of vitrified waste placed in containers and overpacks, encased in exogenous materials (near-field engineered barrier) and ultimately buried in a clay-rich geological formation (far-field barrier). Bentonite, a clay material mostly constituted of smectite, is considered a promising material as an engineered barrier in the context of nuclear waste disposal. The potential of smectite stems from its mechanical self-healing ability, its low hydraulic conductivity and its high sorption capacities, the combination of which is assumed to help prevent or delay radionuclide migration. However, the initial properties of smectite could be altered significantly by storage-induced perturbations. For example, the use of concrete for waste overpacks or the oxidation of pyrite, which is often present as an accessory mineral in the relevant geological environments, can lead to a wide pH range for solutions saturating the clay-barriers.

Substitutions in either tetrahedral or octahedral sheets of the smectite structure induce a permanent negative layer charge that is balanced by the presence of hydrated cations in the interlayer space. The interlayer cation composition of smectite has been studied for many decades as a function of the composition of the solution in contact with clay surfaces (Vanselow, 1932a; Sposito, 1981 and references therein), and the thermodynamics of cation exchange have been developed specifically to model these interlayer cation compositions (Vanselow, 1932a; Sposito, 1977, 1981, 1984; Elprince et al., 1980; Shainberg et al., 1980; Shu-Yuan and Sposito, 1981; Sposito et al., 1981, 1983a, 1983b, 1999; Fletcher and Sposito, 1989; Delville, 1991; Appelo and Postma, 2000). Smectite cation exchange affinities have been established for a wide range of cations including protons, which possibly replace interlayer cations under acidic conditions (Fletcher and Sposito, 1989 and reference therein).

26 For the most common interlayer cations, hydration of homoionic smectites has been
27 extensively studied and it has been shown, most often from the variation of 00 l basal
28 reflection d-spacings, that smectite incorporates H₂O molecules in its interlayers. As a
29 consequence, with increasing relative humidity the smectite structure “swells” in different
30 steps corresponding to the intercalation of 0, 1, 2 or 3 layers of H₂O molecules
31 (Nagelschmidt, 1936; Bradley et al., 1937; Mooney et al., 1952; Norrish, 1954; Walker,
32 1956). From these early studies, it is now accepted that the hydration ability of 2:1
33 phyllosilicates is controlled by factors such as the nature of the interlayer cation and the
34 amount of layer charge and its location (octahedral vs. tetrahedral). These observations have
35 led to different models in which crystalline swelling is controlled by the balance between the
36 repulsive forces between adjacent 2:1 layers and the attractive forces between hydrated
37 interlayer cations and the negatively charged surface of 2:1 layers (Norrish, 1954; Van
38 Olphen, 1965; Kittrick, 1969a, 1969b; Laird, 1996, 1999). The few studies devoted to the
39 hydration of bi-ionic smectites (Glaeser and Méring, 1954; Levy and Francis, 1975), and
40 (Iwasaki and Watanabe, 1988) on (Na, Ca)-smectites and (Mamy and Gaultier, 1979) on (K,
41 Ca)-smectites) have shown that interlayer cations tend to distribute in distinct interlayers
42 leading to a “demixed” state.

43 The present work aims at characterising the hydration state of an initially Ca-
44 saturated montmorillonite as a function of pH in order to better predict smectite reactivity
45 under disturbed chemical conditions, such as those likely to occur in the vicinity of a nuclear
46 waste disposal. For this purpose, the combination of chemical modelling and XRD profile
47 modelling were used to follow the exchange of Ca²⁺ cations by protons under acidic
48 conditions. Specific X-ray diffraction modelling techniques based on a trial-and-error
49 approach were used to refine the early descriptions of smectite hydration by taking into
50 account the possible coexistence in the smectite structure of different layer types, each

51 exhibiting a specific hydration state (Bérend et al., 1995; Cases et al., 1997; Cuadros, 1997;
52 Ferrage et al., 2005a, 2005b). In particular, the likely mutual exclusion of calcium and protons
53 in smectite interlayers and the expected hydration contrast between such calcium- and proton-
54 saturated smectite layers was used to follow the H_3O^+ -for- Ca^{2+} exchange supposed to occur at
55 low pH. The same techniques were also used to assess the possible presence of cation –
56 hydroxide ions pairs under alkaline conditions proposed by Tournassat et al. (2004a, 2004b)
57 and Charlet and Tournassat (2005) on the basis of cation exchange experiments and chemical
58 modelling.

59

60 ----- The following section to be typed in smaller characters -----

61

62 **2. MATERIALS AND METHODS**

63

64 **2.1 Clay material preparation**

65

66 The smectite used for this study was the SWy-2 montmorillonite reference from the
67 Source Clays Repository of The Clay Minerals Society
68 (<http://www.agry.purdue.edu/cjohnston/sourceclays/index.html>) with structural formula
69 (Stucki et al., 1984): $[(\text{Al}_{3.01} \text{Fe}_{0.43} \text{Mg}_{0.56})(\text{Si}_{7.97} \text{Al}_{0.03})\text{O}_{20}(\text{OH})_4] \text{M}^{+0.72}$. Naturally, this
70 montmorillonite is mostly Na-saturated, and exhibits a low octahedral charge deficit and
71 extremely limited tetrahedral substitutions (Mermut and Lagaly, 2001).

72 Size fractionation was performed by centrifugation to obtain a suspension of the
73 $<2 \mu\text{m}$ size fraction. An ion-exchange process was then carried out on this clay separate at
74 room temperature with 1 mol.L^{-1} aqueous saline solution of CaCl_2 . The SWy-2 suspension
75 was shaken mechanically in this saline solution for 24h before separation of the solid fraction

76 by centrifugation and addition of fresh saline solution. This step was repeated three times to
77 ensure complete cation exchange. Excess salts were then washed by four 24h cycles,
78 including sedimentation, removal of the supernatant and re-suspension in deionised water
79 (milli-Q/18.2 M Ω cm⁻¹). The clay content of the final Ca-SWy-2 suspension was found to be
80 ~37g of clay per kg of suspension using the weighing method given by Sposito et al. (1981)
81 and revised by Tournassat et al. (2004a).

82

83 **2.2 Sample preparation**

84

85 Centrifugation tubes were precisely weighed (m_{tube} in g) with a Mettler Toledo
86 AG285 balance. A ~3mL aliquot of the Ca-SWy-2 suspension was introduced into each
87 50 mL centrifuge tube with a calibrated micropipette (V_{susp} , clay content ρ). Variable volumes
88 of Ca(OH)₂ or HCl were then added to reach the desired pH after addition of deionised water
89 to obtain a 40 mL total volume (V_{tot}). The tubes were shaken for three hours. A 15mL
90 suspension aliquot was then collected from each tube, precisely weighed (V_{XRD}) and used for
91 X-ray diffraction (XRD) data collection (see below). The remaining suspension was
92 centrifuged to separate the solution from the clay slurry.

93 An aliquot of supernatant fluid from each tube was further filtered (0.20 μ m) before
94 measuring the pH with a pH-microelectrode (Mettler Toledo, InLab 423). Another aliquot
95 was filtered for Na, Ca, Si, Al, Mg and Fe concentration measurements (C_{sol}^{elt} , where elt
96 represents Ca, Si, etc.) using a Perkin-Elmer Optima 3300 DV inductively coupled plasma
97 atomic emission spectrometer (ICP-AES). Si, Al, Mg and Fe concentrations were measured
98 on a third supernatant aliquot obtained without prior filtration to give the mass of suspended
99 solids in the supernatant as explained in Tournassat et al. (2004a) ($m_{correction}$). On the other
100 hand, the centrifuge tubes containing the clay slurry were weighed precisely ($m_{centrif}$) and 30

101 mL (V_{Amm}) of 1 M ammonium acetate were added to each tube, each tube being precisely
 102 weighed after ammonium acetate addition (m_{Amm}) and shaken for 24h. NH_4^+ cations are meant
 103 to replace Ca^{2+} cations in the smectite interlayer (e.g. Sposito et al., 1981, 1983a, 1983b) and
 104 the subsequent measurement of Ca^{2+} concentration in the supernatant solution leads to the
 105 Calcium Cation Exchange Capacity (Ca-CEC). Since some solution remained in the clay
 106 slurry (V_{slurry}) before the addition of ammonium acetate, the volume of supernatant was equal
 107 to the volume of added ammonium acetate plus this volume of solution in the slurry
 108 ($V_{Amm+slurry}$). Furthermore, the amount of Ca^{2+} present in the remaining slurry solution (C_{sol}^{Ca}
 109 $\times V_{slurry}$) must be subtracted from the amount of Ca in the supernatant ($C_{Amm}^{Ca} \times V_{Amm+slurry}$).
 110 Hence, Ca-CEC is given by the following formula (in eq.kg⁻¹, i.e. in mol of charge per kg of
 111 clay):

$$112 \quad Ca - CEC = 2 \times \frac{C_{Amm}^{Ca} \times V_{Amm+slurry} - C_{sol}^{Ca} \times \left(m_{centrif} - m_{tube} - \left(V_{susp} \times \frac{V_{tot} - V_{XRD}}{V_{tot}} \times \rho \right) \right)}{\left(V_{susp} \times \frac{V_{tot} - V_{XRD}}{V_{tot}} \times \rho \right) - m_{correction}}, \quad (1)$$

$$113 \quad \text{with } V_{Amm+slurry} = \frac{m_{Amm} - m_{tube} - \left(V_{susp} \times \frac{V_{tot} - V_{XRD}}{V_{tot}} \times \rho \right)}{d_{Amm}} \quad (2)$$

114 where volumes (V) are in L, concentrations (C) in mol.L⁻¹, clay content (ρ) in g.L⁻¹ and
 115 masses (m) in g. The density of all solutions was assumed to be equal to 1.0, except for the
 116 density of the 1 M ammonium solution ($d_{Amm} = 1.077$).

117

118 **2.3 Chemical composition modelling**

119

120 The chemical modelling used in this study was performed using the Phreeqc2 code
 121 (Parkhurst and Appelo, 1999), since this versatile computer code is amenable to the various

122 conventions used to describe cation exchange and surface complexation. The model used for
123 cation exchange was similar to that developed by Tournassat et al. (2004a) and only the main
124 concepts and parameters are described to simplify understanding. Cation exchange capacity of
125 montmorillonite originates both from the presence of a permanent negative charge (σ_0) in the
126 clay lattice resulting from octahedral and tetrahedral substitutions and from the presence of
127 broken bonds at the edges of clay platelets, which induces a pH-dependent charge (σ_H). By
128 combining a cation-exchange model based on the Vanselow convention (Vanselow, 1932a;
129 Sposito, 1981) with the pH-dependent charge model developed by Tournassat et al. (2004b)
130 for clay minerals, the evolution of the Ca-CEC value can be modelled as a function of pH.
131 Key parameters are cation exchange selectivity coefficients (K_{int} - Table 1), clay permanent
132 charge (σ_0), structural formula and edge surface area. The latter parameter was considered to
133 be equal to that determined for the fine fraction of the commercial Wyoming bentonite MX80
134 montmorillonite ($8.5 \text{ m}^2.\text{g}^{-1}$, Tournassat et al., 2003). From the adjustment to Ca-CEC data,
135 the σ_0 value was taken to be $0.94 \text{ mol of charge (mol}_c\text{) per kg of clay}$. This value is similar,
136 within error, to the $1.0 \text{ mol}_c.\text{kg}^{-1}$ value calculated from the structural formula. In the model
137 used, a decrease of Ca-CEC was interpreted either as a decrease of σ_H (typically from pH 4 to
138 10 in the present study) or as resulting from H^+ sorption in the interlayer.

139

140 **2.4 X-ray diffraction analysis and profile modelling**

141

142 For XRD analysis, suspension aliquots were poured through a Millipore filter
143 ($0.4\mu\text{m}$) and the clay cake was then laid down on a previously weighed glass slide. The
144 resulting oriented preparations were then dried at room temperature and the mass of smectite
145 on the glass slide was precisely determined. XRD patterns were then recorded using a Bruker
146 D5000 diffractometer equipped with an Ansyco rh-plus 2250 humidity control device coupled

147 to an Anton Paar TTK450 chamber. Data collection was performed at 40% relative humidity
148 (RH) after an homogenisation period of 15 min before the measurement. Experimental
149 measurement parameters were 6s counting time per $0.04^\circ 2\theta$ step. The divergence slit, the two
150 Soller slits, the antiscatter slit and the resolution slit were 0.5° , 2.3° , 2.3° , 0.5° and 0.06° ,
151 respectively. For each sample, XRD patterns were collected over a time span not exceeding
152 one day after glass slide preparation.

153 The algorithms developed initially by Sakharov and Drits (1973), Drits and Sakharov
154 (1976) and more recently by Drits et al. (1997a) and Sakharov et al. (1999) were used to fit
155 experimental XRD profiles over the $2\text{--}50^\circ 2\theta$ $\text{CuK}\alpha$ range using a trial-and-error approach.
156 Instrumental and experimental factors such as horizontal and vertical beam divergences,
157 goniometer radius, length and thickness of the oriented slides were measured and introduced
158 without further adjustment. The mass absorption coefficient (μ^*) was set to $45 \text{ cm}^2 \cdot \text{g}^{-1}$, as
159 recommended by Moore and Reynolds (1997) for clay minerals, whereas the parameter
160 characterising the preferred orientation of the sample (σ^*) was considered as a variable
161 parameter. The z-coordinates for all atoms within the 2:1 layer framework were set as
162 proposed by Moore and Reynolds (1997). The z-coordinates of interlayer species for
163 dehydrated (0W) and mono-hydrated (1W) smectite layers were also set as proposed by
164 Moore and Reynolds (1997), in contrast to those for bi-hydrated (2W) layers, since a more
165 realistic description of the interlayer structure is obtained by assuming a unique plane of H_2O
166 molecules on either side of the central interlayer cation (Ferrage et al., 2005a). The distance
167 along the c^* axis from the interlayer cation plane and the H_2O molecule plane is $\sim 1.2 \text{ \AA}$.

168 Additional variable parameters include the coherent scattering domain size (CSDS)
169 along the c^* -axis, which was characterised by a maximum CSDS, set at 45 layers, and a mean
170 CSDS value (N – Drits et al., 1997b), which was adjusted. In addition, because of the weak
171 bonding between adjacent smectite layers, layer thickness is probably scattered about its

172 average value. This cumulative deviation from strict periodicity, described by Guinier (1964)
173 as a disorder of the second type and detailed later by Drits and Tchoubar (1990), can be
174 considered as strains and was accounted for by introducing a deviation parameter (σ_z). The
175 overall fit quality was assessed using the R_p parameter (Howard and Preston, 1989). This un-
176 weighted parameter was preferred because it is mainly influenced by misfits on the most
177 intense diffraction maxima such as the 001 reflection, which contains essential information on
178 the proportions of the different layer types and on their respective layer thickness

179 The fitting procedure described in detail by Ferrage et al. (2005a) was used for all
180 experimental XRD profiles of exchanged Ca-SWy. Briefly, a main structure, periodic when
181 possible, was used to reproduce as much as possible of the experimental XRD pattern. If
182 necessary, additional contributions to the diffracted intensity were introduced to account for
183 the lack of fit between calculated and experimental patterns. These extra contributions were
184 systematically related to mixed-layered structures (MLS) containing two or three components,
185 randomly interstratified. Up to four structures were necessary to reproduce experimental
186 patterns, because of the very heterogeneous structures observed. However, layers with the
187 same hydration state present in the different MLS contributing to the diffracted intensity were
188 assumed to have identical properties to reduce the number of adjustable parameters.
189 Specifically for a given sample, each given layer type (0W, 1W or 2W layers) was provided
190 with a unique chemical composition, a unique layer thickness, and a unique set of atomic
191 coordinates for all contributions. Similarly, identical values of the σ^* , N and σ_z parameters
192 were used at a given pH value for all MLSs, even though these parameters were nevertheless
193 allowed to vary as a function of pH. The relative proportions of the different MLSs and that of
194 the different layer types in these MLSs were also considered as variable parameters during the
195 fitting procedure.

196 The fitting strategy is illustrated in Figure 1 for the XRD pattern obtained for Ca-
197 Swy-2 equilibrated in deionised water (pH = 6.41). Qualitatively, the experimental pattern
198 exhibits well-defined diffraction maxima forming a rational series with a d_{001} value
199 characteristic of a bi-hydrated state (~ 15.20 Å). However, a significant asymmetry is visible
200 on the high-angle side of the 001 and 003 reflections and on both sides of the 005 reflection
201 (arrows in Figure 1a) as demonstrated by the difference plot between the experimental pattern
202 and that calculated for the contribution of pure bi-hydrated smectite (100% of 2W layers).
203 According to the Méring principle (Méring, 1949), the residual maximum on the high-angle
204 side of the 001 reflection can be attributed to a MLS containing layers with a lower layer
205 thickness in addition to 2W layers. Accordingly, a satisfactory fit ($R_p = 1.45\%$) was obtained
206 when a second contribution ($S2 - S1:S2 = 87:13$), resulting from the random
207 interstratification of 2W, 1W and 0W layers (60%, 30% and 10%, respectively – Figs. 1b, c),
208 was added to the initial contribution (S1), as schematised by the pictogram shown in Figure
209 1d. In this pictogram, the relative proportions of the two MLSs contributing to the diffracted
210 intensity are represented along the vertical axis by their respective surface areas whereas the
211 proportions of the different layer types in each structure are represented on the horizontal axis.
212 Overall, this sample contains 95% of 2W layers, 4% of 1W layers and 1% of 0W layers.

213 One may note that the calculated XRD patterns are not plotted over the low angle
214 region (2θ angles lower than 5°) because the shape of the computed “background” over this
215 angular range is not consistent with that of experimental patterns. The origin of this
216 discrepancy is discussed by Ferrage et al. (2005a) using the recent theoretical developments
217 made by Plançon (2002). These new insights into the real structure of clay aggregates may
218 make it possible to reproduce experimental patterns over this angular range but they would
219 not bring into question the results reported in the present manuscript.

220

221 2.5. Near Infrared Diffuse Reflectance analysis

222

223 Near infrared diffuse reflectance (NIR-DR) spectra were recorded using a Perkin-
224 Elmer 2000 FTIR spectrometer equipped with a deuterated triglycine sulphate (DTGS)
225 detector, a tungsten-halogen source and a quartz beam-splitter. The optical device used is
226 based on the Harrick© equipment. Diffuse reflectance spectra were recorded from 4000 to
227 8000 cm^{-1} with a spectral resolution of 8 cm^{-1} and obtained from the addition of 50 individual
228 scans. Samples were placed into a Harrick© cell in which the temperature and pressure were
229 controlled from 25-100°C and from 10^{-4} - 10^5 Pa, respectively. Sample temperature was
230 measured to an accuracy greater than 0.1°C using a Pt resistance. The spectra of hydrated
231 samples equilibrated at room humidity ($40 \pm 5\%$) were recorded first. The samples were
232 subsequently out-gassed at 60°C for 16 hours under a residual pressure of $5 \cdot 10^{-3}$ Pa by using a
233 two-stage pump comprising a scroll pump and a turbomolecular pump. Two complementary
234 gauges (Pirani and ionisation types) were used to measure the pressure from 10^{-4} Pa to room
235 pressure. Spectra were then recorded at a sample temperature of 25°C under a residual
236 pressure of $5 \cdot 10^{-4}$ Pa. The diffuse reflectance, R , is defined as:

$$237 \quad R = -\log \frac{I_s^D(\sigma)}{I_0^D(\sigma)} \quad (3)$$

238 where I_s^D is the collected diffused irradiance of the sample, I_0^D the collected diffused
239 irradiance of the reference and σ the wavenumber. The reference was taken at 24.8°C from a
240 potassium bromide ground powder subsequently dried under a residual pressure of $5 \cdot 10^{-3}$ Pa.

241 For clay samples, the spectral domain presented in this study can be split into two
242 regions. From 4550 to 5500 cm^{-1} , only H_2O molecules can be observed from the combinations
243 of stretching and bending modes. From 6500 to 7500 cm^{-1} , overtones of stretching modes of
244 all hydroxyl groups, both from interlayer H_2O molecules and from the silicate framework, are

245 visible (Burneau et al., 1990; Madejova et al., 2000b). As fundamental stretching modes of
246 hydroxyl groups have been reported previously over the 3370-3670 cm^{-1} range (Madejova et
247 al., 2000a; Vantelon et al., 2001; Bishop et al., 2002), the frequency range calculated for the
248 first stretching overtone extends from 6575-7175 cm^{-1} , assuming a 82.5 cm^{-1} anharmonicity
249 coefficient for OH groups (Burneau and Carteret, 2000).

250

251 ----- End of the section to be typed in smaller characters -----

252

253

3. RESULTS

254

3.1. Cation concentrations in solution and in the clay interlayer

255

256
257 Concentrations of Ca, Al, Fe and Mg cations in solution are plotted as a function of
258 pH in Figure 2. As observed in earlier studies (Baeyens and Bradbury, 1997; Tournassat et al.,
259 2004a), the concentrations of Al, Fe and Mg in solution increase under low pH conditions as a
260 result of clay dissolution and/or desorption processes. In addition, below a pH value of about
261 3, Ca concentration in solution dramatically increases as the pH decreases, although no Ca is
262 added. At the same time, the apparent amount of Ca sorbed in the clay interlayer decreases
263 (Fig. 3), whereas no other cation, such as Na, Al, Fe or Mg, appears to be sorbed in the
264 interlayer from NH_4^+ exchange experiment results. With decreasing pH, Ca^{2+} is thus certainly
265 replaced by protons in the smectite interlayer as previously hypothesized (Gilbert and
266 Laudelout, 1965; Fletcher and Sposito, 1989; Bradbury and Baeyens, 1997; Tournassat et al.,
267 2004b).

268 Under high pH conditions ($\text{pH} > 12$), the addition of $\text{Ca}(\text{OH})_2$ to the clay suspension
269 leads both to an increase in the Ca concentration in solution and to an increase in the apparent

270 Ca^{2+} sorption on smectite (Figs. 2a, 3). From these observations, and specifically from the
271 concomitant increase in OH^- sorption, Tournassat et al. (2004a, 2004b) have hypothesized the
272 sorption of CaOH^+ ion pairs in the smectite interlayers, as observed for CaCl^+ when ionic
273 strength is high (Sposito et al., 1983a, 1983b; Tournassat et al., 2004b; Ferrage et al., 2005c).
274 However, the concentration of Si in solution decreases simulatenously with the apparent
275 increase of Ca^{2+} sorption on smectite (Fig. 3). This correlation possibly indicates the
276 precipitation of a tobermorite-like Ca-Si phase at high pH (Claret et al., 2002; Tournassat et
277 al., 2004a, 2004b) as discussed below. This hypothesis is also supported by the steady
278 evolution of solution chemistry reported by Tournassat et al. (2004a) when working in a Na^+
279 ionic medium rather than in a Ca^{2+} one. However, sorption of CaOH^+ ion pairs cannot be
280 differentiated from the precipitation of a Ca-Si phase on the sole basis of analytical chemistry
281 experiments. As a consequence, modelling of XRD experiments was carried out in order to
282 characterise the clay structural changes associated with the observed chemical evolutions, and
283 to assess the various hypotheses arising from chemical modelling.

284

285 **3.2. Solid characterisation under acidic conditions**

286 The qualitative observation of the 001 reflection recorded at a constant RH value
287 (40%) for samples equilibrated at different pH values shows a dramatic modification of the
288 smectite hydration state with decreasing pH (Fig. 4a), most probably resulting from the
289 modification of the smectite interlayer composition. Near neutral pH, smectite is mainly bi-
290 hydrated ($d_{001} \sim 15.2 \text{ \AA}$), whereas at low pH values (e.g. 0.14) the presence of protons in the
291 smectite interlayer leads to the shift of the 001 reflection towards lower d_{001} ($\sim 12.6 \text{ \AA}$), which
292 are characteristic of 1W smectites. When decreasing the pH from near neutral condition (pH =
293 6.41), the steady decrease of the 001 reflection intensity and the increase of the asymmetry on
294 its high-angle side are consistent with the continuous incorporation of 1W layers. Extremely

295 heterogeneous structures, most probably corresponding to the interstratification of 2W and
296 1W layers, are observed at intermediate pH values (e.g. 1.41), whereas at lower pH values, the
297 steady increase in the 12.6 Å peak intensity and its sharpening are indicative of a
298 homogeneous 1W state.

299 In the modelling of these experimental XRD patterns, it was assumed that the 1W
300 and 2W layers correspond to smectite layers saturated with protons and Ca^{2+} cations,
301 respectively. This hypothesis is strongly supported by the overwhelming presence of 2W
302 layers in low-charge montmorillonite equilibrated at 40% RH (Ferrage et al., 2005a). In
303 addition, for layers saturated by protons, it was assumed that the layer charge compensation
304 was achieved by H_3O^+ cations, as the difference between H_3O^+ or H^+ cations could not be
305 differentiated from the presence of an additional H_2O molecule on the mid-plane of the H^+ -
306 saturated interlayer. Finally, because X-ray diffraction is only sensitive to the electronic
307 density, a simple calculation of the scattering factor for $\theta = 0$ weighted to the cation valency
308 (η index) shows that it is not possible to differentiate, from the diffracted intensity, between
309 interlayers saturated by Ca^{2+} or H_3O^+ cations. Ca^{2+} cations contain $18e^-$ and therefore $\eta = 9e^-$
310 per charge unit (c.u.) whereas for H_3O^+ ions $\eta = 10 e^-/\text{c.u.}$ This calculation shows that the
311 systematic presence of protons as interlayer cations in 1W, which was initially assumed, will
312 not significantly impact the proportion of the different layer types derived from XRD profile
313 modelling.

314 The calculated profiles are compared to the experimental patterns in Figure 5 and the
315 relative contributions to the diffracted intensity as a function of pH are schematised in Figure
316 6 together with the composition of the associated MLSs. The relative contributions of the
317 different MLSs to the diffracted intensity and their evolution as a function of pH are
318 illustrated in Figure 7 for characteristic XRD patterns. Additional structural parameters, such

319 as the layer thickness of the different layer types, their content of H₂O molecules, the number
320 N of layers building up CSDs, σ^* and σ_z are listed in Table 2.

321 A similar model was found for pH values of 6.41 and 5.98. This model, which is
322 described in the method section, includes both a periodic structure containing only 2W layers
323 and a MLS containing the three layers types (2W:1W:0W ratio 60:30:10 – Figs. 1, 5, 6). The
324 relative abundance of the MLS increases slightly at the expense of the periodic one as pH
325 decreases (Fig. 6). Structure models obtained for the pH values down to 2.88 are quite similar
326 to the previous one, differing only in the presence of a small amount (~2%) of 1W layers in
327 the former periodic structure (Fig. 6). Again, the relative contribution of the most
328 homogeneous structure decreases with decreasing pH. For pH values between 2.46 and 1.93,
329 all attempts to reproduce experimental XRD patterns with two contributions were
330 unsuccessful. As the asymmetry on the high angle side of the 001 reflection becomes more
331 pronounced (Figs. 5, 7) it was necessary to introduce a third contribution. As compared to the
332 previous two contributions, this additional MLS must incorporate a noticeable amount of 1W
333 layers to account for the observed asymmetry. The optimum composition determined for this
334 additional MLS was a 2W:1W:0W ratio of 30:60:10 (Figs. 5, 6). In addition, the composition
335 of the mostly bi-hydrated structure was modified to increase the content of 1W layers up to
336 5% for these pH values between 2.46 and 1.93. The contributions of the different MLS to the
337 XRD pattern recorded for sample pH = 1.93 are illustrated in Figure 7a, in which it is possible
338 to observe the contribution of the additional MLS as a broad modulation at ~14°2 θ .

339 When lowering the pH value to 1.75, it was again necessary to consider an additional
340 contribution to the diffracted intensity in order to satisfactorily fit the experimental XRD
341 pattern (Figs. 5, 6, 7b). In Figure 7b, the maximum at ~14°2 θ now appears as a better-defined
342 peak as compared to Figure 7a, the position of this well-defined maximum indicating that this
343 additional MLS is essentially mono-hydrated. The additional presence of this new MLS

344 (1W:0W ratio 99:1) allows a satisfactory fit to the experimental XRD profile. In Figure 7b,
345 one may also note the presence on the high-angle side of the 001 reflection of broad
346 modulations whose positions are consistent with those of the various MLSs contributing to
347 the calculated intensity. The very heterogeneous structure observed at pH 1.41 (Figs. 6, 7c)
348 was modelled using the same four MLSs as those reported for the previous sample. The
349 composition of these four structures was kept constant for the two samples (pH 1.75 and
350 1.41), the fit of the experimental profile being achieved by varying the relative proportions of
351 the various MLSs (Figs. 5, 6, 7c). A similar model was used to fit the experimental XRD
352 pattern recorded at pH 1.28 (Figs. 5, 6, 7d). In this model, variation of the relative proportion
353 of the different MLSs accounts for most of the profile modification in addition to a limited
354 decrease of the 2W layer content in one of the MLSs. As for the sample at pH = 1.75,
355 modulations, now observed on the low-angle side of the 001 reflection, allow the composition
356 of the different contributions (Fig. 7d) to be defined. On XRD patterns recorded at pH values
357 of 0.98 and 0.14, the 001 reflection appears sharper and more symmetrical, thus allowing a
358 satisfactory fit with only two contributing MLSs (Figs. 5, 6, 7e). The first MLS accounts for
359 most of the diffracted intensity and corresponds to an almost periodic 1W structure, whereas a
360 second MLS (2W:1W:0W ratio 30:40:30) enables the “tails” of the 001 reflection to be fitted
361 (Figs. 6, 7e). With decreasing pH, the content of 2W layers slightly decreases in the latter
362 MLS (Fig. 6).

363 While fitting all the XRD patterns collected under acidic conditions, special attention
364 was paid to keep layer thickness constant for all three layer types (2W, 1W, and 0W – Table
365 2). In addition, for a given sample, the layer and crystal parameters were kept identical for all
366 the MLS, and only the composition and the relative proportions of the different MLSs was
367 allowed to vary. Most structural parameters were found constant with pH, except for the size
368 of CSDs and σ_z , which decrease with decreasing pH, whereas the water content slightly

369 increases in 1W layers (Table 2). The relative proportions of the different layer types are
370 plotted in Figure 8 as a function of pH to highlight the change in hydration state induced by
371 the progressive exchange of H_3O^+ for interlayer cations as pH decreases.

372

373 **3.3. Solid characterisation under basic conditions**

374

375 No significant change in the 001 reflection profile is observed over the basic pH
376 range (Fig. 4b), except for a limited shift of the position from 15.20 Å for near neutral pH
377 conditions to 15.15 Å at pH = 12.62. The extremely similar XRD profiles observed over the
378 whole angular domain (Figs. 4b, 9) are indicative of a constant hydration state over the whole
379 basic pH range. This is confirmed by the comparison between the experimental and calculated
380 XRD patterns (Fig. 9) and by the structure models reported in Figure 10 and further detailed
381 in Table 3. A model similar to that obtained in near neutral conditions (Fig. 1) was used to
382 reproduce the experimental patterns. This model consists of two structures, the first one
383 containing exclusively (6.41-9.59 pH range) or mostly (11.24-12.62 pH range) 2W layers,
384 whereas the three layer types are present in the second MLS (Fig. 10). The relative
385 proportions of the two structures (Fig. 10) and that of the different layer types (Fig. 8) are
386 about constant over the basic pH range. Most structural parameters were also found to be
387 constant over the basic pH range since only a limited increase in the number of layers in the
388 CSDs and a slight decrease of the layer thickness for 2W layers were observed with
389 increasing pH (Table 3).

390

391

4. DISCUSSION

4.1. H_3O^+ -for- Ca^{2+} exchange at low pH

4.1.1. H_3O^+ -for- Ca^{2+} exchange. XRD vs. chemical modelling

Under acidic conditions, a dramatic change in the hydration state is observed as pH decreases from the position of the 001 reflection, which shifts from 15.2 Å (2W layers) under near-neutral conditions to 12.6 Å (1W layers) under low pH conditions. As Ca-saturated low-charge montmorillonite is predominantly bi-hydrated at 40% RH, this modification may be linked to the progressive exchange of protons for interlayer Ca^{2+} that can be deduced from the chemical data (Fig. 3). This data can be simulated with the model given by Tournassat et al. (2004a, 2004b) to deduce the interlayer chemical composition as a function of pH (Fig. 11). The cation exchange reaction selectivity coefficients (K_{int}) reported by Tournassat et al. (2004a) were used (Table 1), whereas the structural CEC was adjusted to a consistent 0.94 eq.kg⁻¹ value; no other parameter was fitted. Interlayer composition modelling confirms that Na, Al, Fe or Mg do not sorb in the interlayer to a significant extent (data not shown). This chemical modelling rather implies the sorption in the interlayer of several species such as Ca^{2+} or H^+ , but also CaCl^+ ion pairs. The incorporation of the latter ion pairs at high ionic strength has been demonstrated by Ferrage et al. (2005c) from the resulting modification of XRD reflection intensity distribution and of the layer thickness value. In the present study, no significant change in the reflection relative intensities is observed and the layer thickness value determined for 2W layers is remarkably constant over the whole low-pH range (Fig. 5 - Table 2). However, the XRD modelling approach is not sensitive enough to detect the low amount of sorbed CaCl^+ species modelled (Fig. 11).

415 The consistency between the XRD modelling and chemical modelling results can be
416 assessed by calculating the hydration state of the sample from the latter results while
417 assuming a fixed hydration state for each interlayer cation. At near-neutral pH (pH = 6.41),
418 interlayers are purely Ca^{2+} -saturated and the hydration state of the sample (2W:1W:0W ratio
419 95:4:1) determined at this pH may be attributed to Ca^{2+} -saturated layers. At extremely low pH
420 (0.14), the 2W:1W:0W ratio is 6:84:10. However, even at this low pH value, a small
421 proportion of Ca^{2+} cations are still sorbed in the smectite interlayer ($0.004 \text{ mol.kg}^{-1}$ at pH =
422 0.14), and the 2W present at this low pH value could possibly be related to remaining Ca^{2+} -
423 saturated layers. H_3O^+ -saturated layers were thus assumed to be either 1W or 0W in a 89:11
424 ratio similar to the 84:10 ratio determined from XRD profile modelling. Using these two
425 hydration states for Ca^{2+} - and H_3O^+ -saturated layers it is possible to calculate from the
426 chemical modelling results the proportion of the different layer types as a function of pH (Fig.
427 12). The excellent agreement found with the data derived from XRD profile modelling
428 confirms that H_3O^+ and Ca^{2+} cations do not coexist in a single interlayer, since this
429 coexistence would induce a significant and strong discrepancy, particularly in the transition
430 region. This segregation of the different cations in different interlayers corresponds to the
431 “demixed state” previously described in heteroionic smectites.

432 Based on water adsorption isotherms, Glaeser and Méring (1954) first suspected the
433 presence of a demixed state in (Na, Ca)-smectites. They demonstrated that Na^+ and Ca^{2+}
434 cations tend to be distributed in different interlayers but the demixing was interpreted as being
435 incomplete for RH values lower than 75%. These results were confirmed by Levy and Francis
436 (1975) using XRD, and Mamy and Gaultier (1979) reported a similar behaviour in (K, Ca)-
437 smectite. More recently, Iwasaki and Watanabe (1988) were able to refine the distribution of
438 Na^+ and Ca^{2+} cations in smectite and smectite-illite MLSs. Assuming that layers with L.Tck.
439 of $\sim 15.0 \text{ \AA}$ and $\sim 12.5 \text{ \AA}$ were Ca- and Na-saturated, respectively, these authors consistently

440 demonstrated that Na^+ and Ca^{2+} cations are distributed in different layers leading to the
441 occurrence of segregated domains.

442

443 4.1.2. Mechanism of H_3O^+ -for- Ca^{2+} exchange

444

445 In the observed H_3O^+ -for- Ca^{2+} exchange, H_3O^+ cations replace Ca^{2+} cations in a layer by layer
446 process, but there is no information on the influence of a given interlayer content on the
447 exchange probability in the next interlayer. The presence of almost periodic 2W and 1W
448 structures systematically suggests a significant segregation in the layer stacking during the
449 exchange process but there is no information directly available on the evolution of the
450 segregation during the process. However, the occurrence probabilities of every layer pair can
451 be calculated from the structure models obtained (Fig. 6 – Drits and Tchoubar, 1990), and it is
452 especially relevant to follow the segregation of Ca-saturated 2W layers by using the
453 segregation index $\text{Sg}(2\text{W})$ defined by Cesari et al. (1965) and more recently by Drits and
454 Tchoubar (1990):

$$455 \quad \text{Sg}(2\text{W}) = 1 - \frac{1 - P_{2\text{W}-2\text{W}}}{1 - W_{2\text{W}}}, \quad (4)$$

456 where $W_{2\text{W}} < P_{2\text{W}-2\text{W}} \leq 1$, $W_{2\text{W}}$ being the relative abundance of 2W layers in the sample and
457 $P_{2\text{W}-2\text{W}}$ the probability for a 2W layer to follow a 2W layer in the layer stacks. $\text{Sg}(2\text{W})$ ranges
458 from 1 for a physical mixture and 0 for a random distribution of layers. To account for the n
459 structures contributing to the diffracted intensity $W_{2\text{W}}$ is expressed as:

$$460 \quad W_{2\text{W}} = \sum_{i=1}^n [\text{Ab.MLS}^i \times W_{2\text{W}}^i] \quad (5)$$

461 where Ab.MLS^i is the relative contribution of the structure MLS^i , and $W_{2\text{W}}^i$ the relative
462 proportion of 2W layers in this structure. For the global sample $P_{2\text{W}-2\text{W}}$ is calculated as:

463
$$P_{2W-2W} = \frac{W_{2W-2W}}{W_{2W}} \quad (6)$$

464 where W_{2W-2W} is the relative abundance of layer pairs constituted of two $2W$ layers. Taking
 465 into account the n structures contributing to the diffracted intensity, this term is calculated as:

466
$$W_{2W-2W} = \sum_{i=1}^n [\text{Ab.MLS}^i \times W_{2W-2W}^i] \quad (7)$$

467 In the present study, layer stacking is random in all MLS contributing to the diffracted
 468 intensity and equation 4 can thus be transformed to:

469
$$\text{Sg}(2W) = 1 - \frac{1 - \sum_{i=1}^n [\text{Ab.MLS}^i \times (W_{2W}^i)^2] / \sum_{i=1}^n [\text{Ab.MLS}^i \times W_{2W}^i]}{1 - \sum_{i=1}^n [\text{Ab.MLS}^i \times W_{2W}^i]}, \quad (8)$$

470 Note that equation 8 is valid only if all MLS contributing to the diffracted intensity are
 471 randomly interstratified. As a function of pH, the calculated $\text{Sg}(2W)$ value ranges from 0.2 to
 472 0.4 whatever the W_{2W} value (Fig. 13). This $\text{Sg}(2W)$ value corresponds to a limited degree of
 473 segregation, and its stability, within error, throughout the whole pH range, including the
 474 H_3O^+ -for- Ca^{2+} exchange zone, indicates that this cation exchange occurs randomly within the
 475 crystals with no influence of the interlayer cation present in the adjacent interlayers.

476

477

478 *4.1.3. XRD characterisation of the resulting solid*

479

480 The XRD profile modelling approach used in the present study allowed all of the
 481 experimental patterns to be reproduced satisfactorily, but it led in a few cases to extremely
 482 heterogeneous structures, as up to four contributions were sometimes necessary to fit XRD
 483 profiles. However, in order to reduce the number of adjustable parameters associated with
 484 these additional contributions, all layers were assumed to have strictly identical properties

485 (layer thickness, σ_z , and H₂O content) in all contributions for a given sample. In addition, the
486 size of the CSDs (N) and the preferred orientation parameter (σ^*) were also identical for the
487 different MLSs contributing to a given XRD pattern. At each pH value, adjustable parameters
488 were thus limited to the composition of the different MLSs, and to their relative proportions.
489 Moreover, when four MLSs were used to fit the experimental XRD patterns (pH = 1.75, 1.48
490 and 1.28 – Fig. 6), these parameters were found to be consistent from one pH value to the
491 next. Two of these four contributions correspond to essentially bi- or mono-hydrated smectite
492 whereas the other two, which account for the heterogeneous layer stacks resulting from the
493 ongoing exchange process, have approximately constant compositions.

494 The decrease in interlayer thickness fluctuation (σ_z parameter) from 0.35 Å for near
495 neutral conditions to 0.23 Å (Table 2) for acidic conditions is associated with the hydration
496 state modification from an essentially bi-hydrated state to an essentially mono-hydrated state.
497 This correlation is consistent with the observations of Ferrage et al. (2005a) on a
498 montmorillonite SWy-1 sample saturated with various monovalent and divalent cations.
499 Indeed, these authors noted that the σ_z parameter is significantly higher (0.25-0.50 Å) when
500 the sample is dominated by 2W layers than when 0W or 1W layers prevail (0.15-0.25 Å).
501 They attributed the higher σ_z values determined for 2W layers to their higher layer thickness,
502 which implies in turn weaker electrostatic interactions between the negatively charged layer
503 and the interlayer cations. As a consequence, the respective positions of two adjacent 2:1
504 layers are weakly constrained and the resulting variation of layer thickness from one
505 interlayer to the adjacent one is enlarged. This phenomenon is likely to occur also for 1W
506 layers, but the lower layer thickness values and the different location of H₂O molecules
507 considerably reduce the screening of electrostatic interactions between the 2:1 layer and the
508 interlayer cations.

509 In addition, Ferrage et al. (2005a) have observed higher σ_z values at the transition
510 between two individual hydration states, possibly as a result of the coexistence, within a
511 single interlayer, of different hydration states resulting in a high degree of fluctuation in the
512 interlayer thickness. On the contrary, in the present study, the σ_z values steadily decrease with
513 decreasing pH even over the H_3O^+ -for- Ca^{2+} exchange zone characterised by heterogeneous
514 structures. Such an even decrease is indicative of the homogeneous hydration state of each
515 interlayer, that is of the mutual exclusion of Ca^{2+} and H_3O^+ cations in a single interlayer,
516 again suggesting a layer-by-layer exchange process leading to a "demixed" state (Glaeser and
517 Méring, 1954; Levy and Francis, 1975; Mamy and Gaultier, 1979; Iwasaki and Watanabe,
518 1988). This is also consistent with the constant layer thickness values determined for both 1W
519 and 2W layers throughout the low-pH range (Table 2).

520 In addition, the number of layers in the CSDS also increases from ~ 8.7 under neutral
521 conditions to ~ 10.0 under acidic conditions. This steady increase with the transition from a bi-
522 hydrated state to a mono-hydrated state is consistent with the decreasing N values determined
523 by Ferrage et al. (2005a, 2005b) for smectite XRD at high RH values when 2W layers prevail,
524 in agreement with Mystkowski et al. (2000). This evolution can possibly be related to the
525 breakdown of crystals resulting from the swelling of specific interlayers, which statistically
526 decreases the crystallite thickness with increasing RH.

527

528 **4.2. Assessment of the presence of CaOH^+ ion pairs in the alkaline pH range**

529

530 The possibility of interlayer CaOH^+ ion pairs compensating the octahedral charge
531 under alkaline conditions has been evoked on the basis of cation exchange experiments and
532 chemical modelling to model the apparent increase of sorbed Ca^{2+} at high pH values (Fig. 3 –
533 Charlet and Tournassat, 2004; Tournassat et al., 2004a, 2004b). However, Ferrage et al.

534 (2005c) has shown that the presence of CaCl^+ ion pairs similarly evoked for samples
535 equilibrated with saline solutions (Sposito et al., 1983a 1983b; Tournassat et al., 2004b)
536 induces significant modification of the experimental XRD patterns. These modifications
537 affect (i) the intensity ratio between the reflections, as a result of the increase in the electronic
538 density in the interlayer, (ii) the homogeneity of layer thickness (lower σ_z values), and (iii) the
539 hydration properties of exchanged smectite, in particular by lowering the relative humidity
540 value necessary for the bi- to mono-hydrated transition. In addition, the presence of CaCl^+ ion
541 pairs may be assessed using NIR-DR spectroscopy from its influence on interlayer H_2O
542 vibration bands. The methodology developed by Ferrage et al. (2005c) to assess the presence
543 of CaCl^+ ion pairs in the interlayer of montmorillonite, was applied in the present study to
544 assess the possible presence of CaOH^+ ion pairs under high pH conditions.

545

546 *4.2.1. XRD characterisation of the solid*

547

548 Under alkaline conditions, no significant modification of the experimental XRD
549 patterns is observed as a function of pH and the resulting structure models are similar over the
550 whole pH range investigated (pH 6.41-12.62). However, it was not possible to keep the layer
551 thickness of 2W layers constant and a very limited variation was observed (from 15.17 to
552 15.15 Å), whereas other structural parameters (σ^* , σ_z , N or water content) were found to be
553 constant over the whole pH range (Table 3). If CaOH^+ ion pairs were sorbed in the smectite
554 interlayers at high pH values, relative reflection intensities in the high-angle region would be
555 significantly affected, even though the electron density is lower for CaOH^+ ion pairs ($28e^-$
556 /c.u.) than for CaCl^+ ion pairs ($36 e^-$ /c.u.). The impact of CaOH^+ ion pairs on XRD profiles is
557 illustrated in Figure 14, which shows two patterns calculated for the sample at pH = 12.62.
558 The first pattern (solid line) is calculated assuming only Ca^{2+} as the interlayer cation, whereas

559 the second pattern (grey line) is calculated with CaOH^+ ion pairs as compensating species, all
560 other structure parameters being kept constant. The presence of CaOH^+ ion pairs is clearly
561 demonstrated by the increase in the 002 and 003 reflection intensity. On the contrary, all
562 experimental profiles displayed in Figure 9 are similar, and the presence of interlayer CaOH^+
563 ion pairs may be dismissed.

564

565 4.2.2. NIR-DR spectroscopy characterisation of the solid

566

567 NIR-DR spectroscopy was used as an independent, complementary technique to
568 investigate the possibility of CaOH^+ sorption in montmorillonite interlayer under high-pH
569 conditions. This technique allows the amount of water and its local interaction with interlayer
570 species to be studied. In addition, the high sensitivity of infrared spectroscopy for hydroxyls
571 should allow the detection of partial CaOH^+ -for- Ca^{2+} exchange, especially in the hydroxyl
572 band region. In their study, Ferrage et al. (2005c) showed that when the octahedral charge is
573 compensated by CaCl^+ ion pairs instead of Ca^{2+} cations, the main modifications to NIR-DR
574 spectra are: (i) for hydrated samples (40% RH), an increased amount of H_2O induced by the
575 increased amount of interlayer cationic species and (ii) for out-gassed samples, a shift of H_2O
576 vibration bands induced by the perturbation of the H_2O - Ca^{2+} interaction by Cl^- anions. On the
577 contrary, the NIR-DR spectra recorded at 0% and ~40% RH for samples obtained at pH 6.41
578 and 12.62 (Figs. 15, and 16, respectively) are almost identical to each other, whatever the data
579 collection conditions. In the spectral domain of combinations of H_2O molecules (4550-5500
580 cm^{-1}), the band at 5240-5250 cm^{-1} can be assigned to H_2O molecules perturbed by interlayer
581 cations. At 0% RH, this band is still visible, indicating the presence of H_2O molecules despite
582 the out-gassing conditions (Fig. 15). The residual difference between the spectra recorded for
583 samples obtained at pH 6.41 and 12.62 (Fig. 15c) reveals a slightly higher amount of H_2O

584 molecules in the sample at pH = 6.41. This difference, which probably results from not
585 strictly identical out-gassing conditions and H₂O desorption kinetics for the two experiments,
586 again pleads against the presence of CaOH⁺ ion pairs in the smectite interlayer under high-pH
587 conditions. In the spectral domain of overtones (6500-7500 cm⁻¹), similar bands are observed
588 for the two samples at 6910 and 7090 cm⁻¹.

589 As observed under out-gassed conditions, the two spectra recorded at 40% RH for
590 the same samples are similar (Fig. 16), whereas several modifications between the two sets of
591 spectra result from the presence of H₂O molecules. At 40% RH, a shoulder located at
592 ~5130 cm⁻¹ is observed for the two samples in the region of combinations (Fig. 16a,b) and the
593 band observed at 5240 cm⁻¹ under out-gassed conditions is shifted to 5250 cm⁻¹. These two
594 bands account for the presence of H₂O molecules weakly adsorbed on interlayer cations and
595 H-bonded vibrations. Overtones of H₂O molecules and hydroxyl stretching are also shifted by
596 the presence of water and are observed at 6830 and 7080 cm⁻¹ for the two hydrated samples.
597 As for spectra recorded under out-gassed conditions, the difference between the two spectra
598 (Fig. 16c) reveals that the amount of H₂O is again slightly higher in the sample prepared at
599 pH = 6.41 as compared to the one obtained under high-pH conditions. This difference most
600 probably results from slightly different experimental conditions rather than from a contrasting
601 interlayer composition, again pleading against the presence of CaOH⁺ ion pairs in the smectite
602 interlayer under high-pH conditions.

603

604 *4.2.3. Implications on the modelling of the analytical chemistry results for the alkaline pH* 605 *range*

606

607 As discussed above, XRD and NIR-DR spectroscopy results consistently show that
608 CaOH⁺ ion pairs do not enter smectite interlayers at high pH in a calcium cation background.

609 Hence, the analytical chemistry results need to be modelled without the contribution of such
610 ion pairs and the modelling results from Tournassat et al. (2004b), accounting for the sorption
611 of CaOH^+ pairs, must be re-examined.

612 Ca-CEC, the apparent CEC in a Ca^{2+} cation background (in eq.kg^{-1} or $\text{mol}_c.\text{kg}^{-1}$), is
613 given by the following equation:

$$614 \quad \text{Ca-CEC} \Leftrightarrow 2 \times \text{Ca}_{\text{sorbed}} \quad (9)$$

615 where $\text{Ca}_{\text{sorbed}}$ is the amount of Ca sorbed on clay surfaces in mol.kg^{-1} . If one assumes that
616 CaOH^+ is the only compensating species in smectite interlayers at high pH, the reaction taking
617 place during the Ca-CEC measurement experiment is:



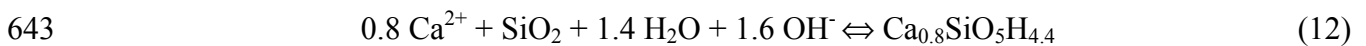
619 where X^- represents one mole of the exchanger phase. Then, $\text{Ca}_{\text{sorbed}} = 2 [\text{Ca}^{2+}]_1/\rho$, where
620 $[\text{Ca}^{2+}]_1$ is the concentration of Ca^{2+} released in solution by reaction 10 and determined
621 experimentally (Sposito et al., 1981, 1983a). The presence of CaOH^+ in exchange position
622 thus leads to an apparent increase in the Ca-CEC as each Ca in solution is converted to two
623 structural charges in the calculation, even though one CaOH^+ equilibrates only one structural
624 charge (Sposito et al., 1983a, 1983b).

625 CaOH^+ exchange also leads to the net consumption of one OH^- per sorbed CaOH^+ ,
626 leading to a one-to-one correlation between the change of apparent surface charge
627 (disappearance of OH^- in eq.kg^{-1}) and that of Ca-CEC (in eq.kg^{-1} – reaction 11 – Tournassat et
628 al., 2004a, 2004b):



630 Hence, reaction 11 could explain almost perfectly the increase in Ca-CEC as a
631 function of pH in the present study and the Ca^{2+} -CEC vs. "sorbed" OH^- stoichiometry
632 observed in the study of Tournassat et al. (2004a, 2004b). This assumption is in contradiction
633 with the experimental evidence deduced from XRD and NIR-DR spectroscopy results.

634 As precipitation of a Ca-Si phase can be an alternative explanation for the apparent
635 increase in Ca sorption and for the decrease in Si concentration occurring under high-pH
636 conditions, the saturation index of many Calcium-Silicate-Hydrate (CSH – HATCHES, 1998)
637 were calculated as a function of pH for the solution composition reported in the present study
638 and in that of Tournassat et al. (2004a). Among the results listed in Table 4, it is possible to
639 note that both CSH 0.8 and CSH 1.1 (HATCHES, 1998) are oversaturated with respect to the
640 chemical conditions prevailing in solution. Since CSH 0.8 is closer from its equilibrium ion
641 activity product than CSH 1.1, the former phase is more likely to precipitate, as described in
642 the following reaction:



644 The precipitate would remain in the clay slurry during the centrifugation step before
645 addition of NH_4^+ . This addition desorbs Ca^{2+} from the interlayer and also induces the
646 dissolution of the CSH 0.8 phase as a result of the pH decrease resulting from the dilution of
647 the alkaline solution in contact with the clay slurry. In turn, this dissolution leads to the
648 release of Ca^{2+} in solution and to the observed apparent increase in the Ca-CEC. Since
649 reaction 12 leads to a one-to-one correlation between the change of apparent surface charge
650 and that of Ca-CEC (disappearance of 1.6 mol_c of OH^- and $0.8 \times 2 = 1.6$ mol_c of Ca^{2+}), it may
651 equally account for the observed Ca^{2+} -CEC vs. "sorbed" OH^- stoichiometry.

652

653 **5. CONCLUSIONS**

654

655 The present study focuses on the modification to the hydration state occurring in Ca-
656 SWy-2 montmorillonite as a function of pH. Under acidic conditions, a transition from bi-
657 hydrated to mono-hydrated state was observed, occurring as the result of a H_3O^+ -for- Ca^{2+}
658 exchange in the smectite interlayer. XRD profile modelling was successfully applied to

659 determine the proportion of the different layer types in the reacted samples, even for
660 extremely heterogeneous hydration states. The proportion of layers obtained was consistent
661 with that derived from chemical modelling, confirming the latter results and demonstrate the
662 ability of these two independent methods to accurately characterise chemical/structural
663 modifications in smectite interlayers. In addition, the exchange between Ca^{2+} cations and
664 H_3O^+ ions has been shown to occur as a layer-by-layer process, taking place randomly in the
665 layer stack.

666 Under high-pH conditions, the possible presence of CaOH^+ ion pairs in the smectite
667 interlayer is proven to be false from results obtained both by XRD profile modelling and by
668 NIR-DR spectroscopy. As a consequence, the apparent increase in Ca sorption and the
669 decrease in Si concentration occurring under high-pH conditions probably result most likely
670 from the precipitation of a CSH phase, which is thermodynamically favoured.

671
672 *Acknowledgements* – The results presented in the present article were collected during a Ph.D.
673 thesis granted by ANDRA (French National Agency for Nuclear Waste Disposal). ANDRA is
674 thanked for its permission to publish this manuscript, and the authors acknowledge its
675 financial support. The French Geological Survey (BRGM) is acknowledged for its editorial
676 financial support. EF is grateful to Pr. Boris A. Sakharov for fruitful discussions during XRD
677 profile modelling. The manuscript was improved by the constructive reviews of two
678 anonymous reviewers and AE Garrison Sposito, and by the remarks of Emmanuel Jacquot on
679 an early version of the manuscript.

680

REFERENCES

- 680
681
- 682 Appelo, C.A.J. and Postma, D. (2000) *Geochemistry, Groundwater and Pollution*, Rotterdam
683 press, 536pp.
- 684 Baeyens, B. and Bradbury, M.H. (1997) A mechanistic description of Ni and Zn sorption on
685 Na-montmorillonite. Part I: Titration and sorption measurements. *J. Contam. Hydrol.*
686 **27**, 199-222.
- 687 Bérend, I., Cases, J.M., François, M., Uriot, J.P., Michot, L.J., Masion, A. and Thomas, F.
688 (1995) Mechanism of adsorption and desorption of water vapour by homoionic
689 montmorillonites: 2. the Li⁺, Na⁺, K⁺, Rb⁺ and Cs⁺ exchanged forms. *Clays Clay*
690 *Miner.* **43**, 324-336.
- 691 Bishop, J., Murad, E. and Dyar, M.D. (2002) The influence of octahedral and tetrahedral
692 cation substitution on the structure of smectites and serpentines as observed through
693 infrared spectroscopy. *Clay Miner.* **37**, 361-628.
- 694 Bradbury, M.H. and Baeyens, B. (1997) A mechanistic description of Ni and Zn sorption on
695 Na-montmorillonite. Part II: modeling. *J. Contam. Hydrol.* **27**, 223-248.
- 696 Bradley, W.F., Grim, R.E. and Clark, G.F. (1937) A study of the behavior of montmorillonite
697 on wetting. *Z. Kristallogr.* **97**, 260-270.
- 698 Burneau, A., Barrès, O., Gallas, J.P. and Lavalley, J.C. (1990) Comparative study of the
699 surface hydroxyl groups of fumed and precipitated silicas. 2. Characterization by
700 infrared spectroscopy of the interaction with water. *Langmuir* **6**, 1364-1372.
- 701 Burneau, A. and Carteret, C. (2000) Near infrared and ab initio study of the vibrational modes
702 of isolated silanol on silica. *Phys. Chem. Chem. Phys.* **2**, 3217-3226.
- 703 Cases, J.M., Bérend, I., François, M., Serekova, Uriot, J.P., Michot, L.J. and Thomas, F.
704 (1997) Mechanism of adsorption and desorption of water vapour by homoionic

705 montmorillonite: 3. the Mg²⁺, Ca²⁺, Sr²⁺ and Ba²⁺ exchanged forms. *Clays Clay*
706 *Miner.* **45**, 8-22.

707 Cesari, M., Morelli, G.L. and Favretto, L. (1965) The determination of the type of stacking in
708 mixed-layer clay minerals. *Acta Cryst.* **18**, 189-196.

709 Charlet, L. and Tournassat, C. (2005) Fe(II)-Na(I)-Ca(II) cation exchange on montmorillonite
710 in chloride medium; evidence for preferential clay adsorption of chloride – metal ion
711 pairs in seawater. *Aquat. Geochem.* (in press).

712 Claret, F., Bauer, A., Schafer, T., Griffault, L. and Lanson, B. (2002) Experimental
713 Investigation of the interaction of clays with high-pH solutions: a case study from the
714 Callovo-Oxfordian formation, Meuse-Haute Marne underground laboratory (France).
715 *Clays Clay Miner.* **50**, 633-646.

716 Cuadros, J. (1997) Interlayer cation effects on the hydration state of smectite. *Am. J. Sci.* **297**,
717 829-841.

718 Delville, A. (1991) Modeling the clay-water interface. *Langmuir* **7**, 547-555.

719 Drits, V.A. and Sakharov, B.A. (1976) *X-Ray structure analysis of mixed-layer minerals.*
720 Dokl. Akad. Nauk SSSR, Moscow, 256 pp.

721 Drits, V.A. and Tchoubar, C. (1990) *X-ray diffraction by disordered lamellar structures:*
722 *Theory and applications to microdivided silicates and carbons.* Springer-Verlag,
723 Berlin, 371 pp.

724 Drits, V.A., Sakharov, B.A., Lindgreen, H. and Salyn, A. (1997a) Sequential structure
725 transformation of illite-smectite-vermiculite during diagenesis of Upper Jurassic shales
726 from the North Sea and Denmark. *Clay Miner.* **32**, 351-371.

727 Drits, V.A., Srodon, J. and Eberl, D.D. (1997b) XRD measurement of mean crystallite
728 thickness of illite and illite/smectite: reappraisal of the kubler index and the scherrer
729 equation. *Clays Clay Miner.* **45**, 461-475.

730 Elprince, A.M., Vanselow, A.P. and Sposito, G. (1980) Heterovalent, ternary cation exchange
731 equilibria: NH_4^+ - Ba^{2+} - La^{3+} exchange on montmorillonite. *Soil Sci. Soc. Am. J.* **44**,
732 964-969.

733 Ferrage, E., Lanson, B., Sakharov, B.A. and Drits, V.A. (2005a) Investigation of smectite
734 hydration properties by modeling of X-ray diffraction profiles. Part 1. Montmorillonite
735 hydration properties. *Amer. Mineral.*, (accepted).

736 Ferrage, E., Lanson, B., Sakharov, B.A., Jacquot, E., Geoffroy, N. and Drits, V.A. (2005b)
737 Investigation of smectite hydration properties by modeling of X-ray diffraction
738 profiles. Part 2. Influence of layer charge and charge location, (in preparation).

739 Ferrage, E., Tournassat, C., Rinnert, E., Charlet, L. and Lanson, B. (2005c) Experimental
740 evidence for calcium-chloride ion pairs in the interlayer of montmorillonite. A XRD
741 profile modelling approach. *Clays Clay Miner.* (accepted).

742 Fletcher, P. and Sposito, G. (1989) The chemical modeling of clay/electrolyte interactions for
743 montmorillonite. *Clay Miner.* **24**, 375-391.

744 Gilbert, M. and Laudelout, H. (1965) Exchange properties of hydrogen ions in clays. *Soil Sci.*
745 **100**, 157.

746 Glaeser, R. and Méring, J. (1954) Isothermes d'hydratation des montmorillonites bi-ioniques
747 (Ca, Na). *Clay Mineral. Bull.* **2**, 188-193.

748 Guinier, A. (1964) *Théorie et technique de la radiocristallographie*. Dunod, Paris, 740 pp.

749 HATCHES (1998) Harwell/Nirex thermodynamic database for chemical equilibrium studies.

750 Howard, S.A. and Preston, K.D. (1989) Profile fitting of powder diffraction patterns. Pp. 217-
751 275 in: *Modern Powder Diffraction* (D.L. Bish and J.E. Post, editors). Reviews in
752 Mineralogy **20**, Mineralogical Society of America, Washington D.C.

753 Iwasaki, T. and Watanabe, T. (1988) Distribution of Ca and Na ions in dioctahedral smectites
754 and interstratified dioctahedral mica/smectites. *Clays Clay Miner.* **36**, 73-82.

- 755 Kittrick, J.A. (1969a) Interlayer forces in montmorillonite and vermiculite. *Soil Sci. Soc. Am.*
756 *J.* **33**, 217-222.
- 757 Kittrick, J.A. (1969b) Quantitative evaluation of the strong-force model for expansion and
758 contraction of vermiculite. *Soil Sci. Soc. Am. J.* **33**, 222-225.
- 759 Laird, D.A. (1996) Model for crystalline swelling of 2:1 phyllosilicates. *Clays Clay Miner.*
760 **44**, 553-559.
- 761 Laird, D.A. (1999) Layer charge influences on the hydration of expandable 2:1
762 phyllosilicates. *Clays Clay Miner.* **47**, 630-636.
- 763 Levy, R. and Francis, C.W. (1975) Demixing of sodium and calcium ions in montmorillonite
764 crystallites. *Clays Clay Miner.* **23**, 475-476.
- 765 Madejova, J., Bujdak, J., Petit, S. and Komadel, P. (2000a) Effects of chemical composition
766 and temperature of heating on the infrared spectra of Li-saturated dioctahedral
767 smectites. (I) Mid-infrared region. *Clay Miner.* **35**, 739-751.
- 768 Madejova, J., Bujdak, J., Petit, S. and Komadel, P. (2000b) Effects of chemical composition
769 and temperature of heating on the infrared spectra of Li-saturated dioctahedral
770 smectites. (II) Near-infrared region. *Clay Miner.* **35**, 753-761.
- 771 Mamy, J. and Gaultier, J.P. (1979) Etude comparée de l'évolution des montmorillonites
772 biioniques K-Ca de Camp-Berteaux et du Wyoming sous l'effet des cycles
773 d'humectation et de dessiccation. *Clay Miner.* **14**, 181-192.
- 774 Méring, J. (1949) L'interférence des rayons-X dans les systèmes à stratification désordonnée.
775 *Acta Cryst.* **2**, 371-377.
- 776 Mermut, A.R. and Lagaly, G. (2001) Baseline studies of the clay minerals society source
777 clays: layer-charge determination and characteristics of those minerals containing 2:1
778 layers. *Clays Clay Miner.* **49**, 393-397.

779 Mooney, R.W., Keenan, A.G. and Wood, L.A. (1952) Adsorption of water vapor by
780 montmorillonite. II. Effect of exchangeable ions and lattice swelling as measured by
781 X-ray diffraction. *J. Am. Chem. Soc.* **74**, 1331-1374.

782 Moore, D.M. and Reynolds, R.C., Jr (1997) *X-ray Diffraction and the Identification and*
783 *Analysis of Clay Minerals*. Oxford University Press, Oxford and New York, 322pp pp.

784 Mystkowski, K., Srodon, J. and Elsass, F. (2000) Mean thickness and thickness distribution of
785 smectite crystallites. *Clay Miner.* **35**, 545-557.

786 Nagelschmidt, G. (1936) The structure of montmorillonite. *Z. Kristallogr.* **93**, 481-487.

787 Norrish, K. (1954) The swelling of montmorillonite. *Disc. Farad. Soc.* **18**, 120-134.

788 Parkhurst, D.L. and Appelo, C.A.J. (1999) Phreeqc2 user's manual and program U.S.
789 Geological Survey.

790 Plançon, A. (2002) New modeling of X-ray diffraction by disordered lamellar structures, such
791 as phyllosilicates. *Amer. Mineral.* **87**, 1672-1677.

792 Sakharov, B.A. and Drits, V.A. (1973) Mixed-layer kaolinite-montmorillonite: a comparison
793 observed and calculated diffraction patterns. *Clays Clay Miner.* **21**, 15-17.

794 Sakharov, B.A., Lindgreen, H., Salyn, A. and Drits, V.A. (1999) Determination of illite-
795 smectite structures using multispecimen X-Ray diffraction profile fitting. *Clays Clay*
796 *Miner.* **47**, 555-566.

797 Shainberg, I., Oster, J.D. and Wood, J.D. (1980) Sodium/calcium exchange in
798 montmorillonite and Illite suspension. *Soil Sci. Soc. Am. J.* **44**, 960-964.

799 Shu-Yuan, C. and Sposito, G. (1981) The thermodynamics of ternary cation exchange
800 systems and the subregular model. *Soil Sci. Soc. Am. J.* **45**, 1084-1089.

801 Sposito, G. (1977) The Gapon and Vanselow selectivity coefficients. *Soil Sci. Soc. Am. J.* **41**,
802 1205-1206.

803 Sposito, G. (1981) *The thermodynamics of soil solution*. Oxford University Press, New
804 Yorkpp.

805 Sposito, G. (1984) *Surface chemistry of soils*. Oxford University press, New York, 223 pp.

806 Sposito, G., Holtzclaw, K.M., Johnston, C.T. and Le Vesque, C.S. (1981) Thermodynamics of
807 sodium-copper exchange on Wyoming bentonite at 298 K. *Soil Sci. Soc. Am. J.* **45**,
808 1079-1084.

809 Sposito, G., Holtzclaw, K.M., Charlet, L., Jouany, C. and Page, A.L. (1983a) Sodium-calcium
810 and sodium-magnesium exchange on Wyoming bentonite in perchlorate and chloride
811 background ionic media. *Soil Sci. Soc. Am. J.* **47**, 51-56.

812 Sposito, G., Holtzclaw, K.M., Jouany, C. and Charlet, L. (1983b) Cation selectivity in
813 sodium-calcium, sodium-magnesium, and calcium-magnesium exchange on Wyoming
814 bentonite at 298 K. *Soil Sci. Soc. Am. J.* **47**, 917-921.

815 Sposito, G., Skipper, N.T., Sutton, R., Park, S. and Soper, A.K. (1999) Surface geochemistry
816 of the clay minerals. *Proceedings of the National Academy of Sciences of the United*
817 *States of America*, **96**, 3358-3364.

818 Stucki, J.W., Golden, D.C. and Roth, C.B. (1984) Effects of reduction and reoxidation of
819 structural iron on the surface charge dissolution of dioctahedral smectites. *Clays Clay*
820 *Miner* **32**, 350-356.

821 Tournassat, C., Neaman, A., Villieras, F., Bosbach, D. and Charlet, L. (2003)
822 Nanomorphology of montmorillonite particles: Estimation of the clay edge sorption
823 site density by low-pressure gas adsorption and AFM observations. *Amer. Mineral.* **88**,
824 1989-1995.

825 Tournassat, C., Greneche, J.M., Tisserand, D. and Charlet, L. (2004a) The titration of clay
826 minerals. Part I. Discontinuous backtitration technique combined to CEC
827 measurements. *J. Colloid Interf. Sci.* **273**, 224-233.

- 828 Tournassat, C., Ferrage, E., Poinsignon, C. and Charlet, L. (2004b) The titration of clay
829 minerals. Part II. Structural-based model and implications for clay reactivity. *J.*
830 *Colloid Interf. Sci.* **273**, 234-246.
- 831 Van Olphen, H. (1965) Thermodynamics of interlayer adsorption of water in clays. *J. Colloid*
832 *Interf. Sci.* **20**, 822-837.
- 833 Vanselow, A.P. (1932a) Equilibria of the base-exchange reaction of bentonites, permutites,
834 Soil colloids and zeolites. *Soil Sci.* **33**, 95-113.
- 835 Vantelon, D., Pelletier, M., Michot, L.J., Barres, O. and Thomas, F. (2001) Fe, Mg and Al
836 distribution in, the octahedral sheet of montmorillonites. An infrared study in the OH-
837 bending region. *Clay Miner.* **36**, 369-379.
- 838 Walker, G.F. (1956) The mechanism of dehydration of Mg-vermiculite. *Clays Clay Miner.* **4**,
839 101-115.
- 840

FIGURE CAPTIONS

840
841
842
843
844
845
846
847
848
849
850
851
852
853
854
855
856
857
858
859
860
861
862

Fig. 1. Schematic description of the strategy used to fit experimental XRD patterns (see text for details). Intensities in the high-angle region ($10\text{-}50^\circ 2\theta$) are enlarged ($\times 10$) compared to the low-angle region ($4\text{-}10^\circ 2\theta$). Qz indicates the presence of quartz. **a)** Experimental pattern of Ca-SWy-2 sample equilibrated in deionised water (pH = 6.41) is shown as crosses whereas the XRD pattern calculated for a periodic bi-hydrated structure (100% bi-hydrated layers – 2W) is shown as a solid line. **b)** Addition of a mixed layer structure (solid grey line) with a 60:30:10 ratio between 2W:1W:0W layers. **c)** Optimum fit to the experimental pattern corresponding to the combination of the above two structures in a 87:13 ratio (solid line). **d)** Schematic representation of the structure model used to fit the experimental XRD pattern. Relative proportions, expressed in wt%, of the two elementary contributions are plotted on the y-axis whereas their compositions (relative proportions of the different layer types) are plotted on the x-axis. Light grey, dark grey and solid bars represent 0W, 1W, and 2W layers, respectively.

Fig. 2. Calcium concentration in solution equilibrated with clay suspension as a function of pH (**a**). Aluminium, iron and magnesium concentrations in solution equilibrated with clay suspension as a function of pH (**b**).

Fig. 3. Apparent amount of calcium sorbed on smectite and Si concentration in solution as a function of pH.

Fig. 4. Evolution of the 001 reflection of equilibrated Ca-SWy-2 as a function of pH. **a)** Under acidic conditions. **b)** Under alkaline conditions.

863 **Fig. 5.** Comparison between experimental and calculated XRD patterns as a function of pH
864 under acidic conditions. Experimental XRD patterns are shown as crosses whereas
865 the optimum fits are shown as solid lines.

866 **Fig. 6.** Structure models obtained from XRD profile modelling for samples prepared under
867 acidic conditions. Symbols and notations as for Figure 1d.

868 **Fig. 7.** Respective contributions of the various mixed-layer structures (MLSs) to the
869 calculated profiles. Intensities in the high angle region ($10\text{-}50^\circ 2\theta$) are enlarged ($\times 10$)
870 as compared to the lower angle region ($2\text{-}10^\circ 2\theta$). The different MLSs are shown as
871 bold, light grey, dark grey and thin solid lines, experimental data are shown as
872 crosses. **a)** pH = 1.93. **b)** pH = 1.75. **c)** pH = 1.41. **d)** pH = 1.28. **e)** pH = 0.14.

873 **Fig. 8.** Relative proportion of the different layer types obtained from XRD profile modelling
874 as a function of pH. Solid squares: 2W layers; dark grey squares: 1W layers; light
875 grey squares: 0W layers.

876 **Fig. 9.** Comparison between experimental and calculated XRD patterns as a function of pH
877 under alkaline conditions. Symbols as for Figure 5.

878 **Fig. 10.** Structure models obtained from XRD profiles modelling for samples prepared under
879 alkaline conditions. Symbols and notations as for Figure 1d.

880 **Fig. 11.** Apparent amount of Ca sorbed on smectite as a function of pH. Experimentally
881 determined values: open squares. Results of the exchange modelling using the
882 modelling approach developed by Tournassat et al. (2004a) are shown as bold solid
883 lines (Ca^{2+}), dashed lines (H^+), and solid lines (CaCl^+).

884 **Fig. 12.** Comparison between the relative abundance of the different layer types obtained
885 from XRD profile modelling (symbols) and that derived from chemical modelling
886 (solid lines), as a function of pH. Light grey, dark grey and black colours correspond
887 to 0W, 1W, and 2W layers, respectively

888 **Fig. 13.** Relative abundance of 2W layers obtained from XRD profile modelling (solid
889 squares) and segregation index of 2W layers ($Sg(2W)$ – solid diamonds) as a
890 function of pH under acidic conditions.

891 **Fig. 14.** Comparison between the experimental pattern of the sample prepared at pH = 12.62
892 (crosses) with those calculated Ca^{2+} cations (solid line) or $CaOH^+$ ion pairs (solid
893 grey line) as the sole charge compensating species.

894 **Fig. 15.** NIR-DR spectra of out-gassed samples. **a)** Sample prepared under near-neutral
895 conditions (pH = 6.41). **b)** Sample prepared under alkaline conditions (pH = 12.62).
896 **c)** Difference between the above two spectra ($c = b - a$).

897 **Fig. 16.** NIR-DR spectra of hydrated samples ($RH = 40 \pm 5\%$). **a)** Sample prepared under
898 near-neutral conditions (pH = 6.41). **b)** Sample prepared under alkaline conditions
899 (pH = 12.62). **c)** Difference between the above two spectra ($c = b - a$).

Table 1. Cation exchange reaction selectivity coefficients (K_{int}) used for chemical composition modelling.

Exchange reactions	$\log K_{int}$
$2 \text{HX} + \text{Ca}^{2+} \Leftrightarrow \text{CaX}_2 + 2 \text{H}^+$	0.4 [§]
$\text{HX} + \text{CaCl}^+ \Leftrightarrow \text{CaClX} + \text{H}^+$	2.5 [§]

[§] from Tournassat et al. (2004a)

Table 2. Optimum structure parameters determined from the fitting of XRD profiles recorded for samples prepared under acidic conditions.

pH	LT 2W	LT 1W	LT 0W	N	σ^*	σ_z	nH ₂ O 2W	nH ₂ O 1W
6.41	15.18	12.60	10.00	8.7	6.5	0.35	2×3.2	3.2
5.98	15.18	12.60	10.00	8.7	6.3	0.35	2×3.2	3.2
4.73	15.18	12.60	10.00	8.8	6.3	0.35	2×3.2	3.2
2.88	15.18	12.60	10.00	8.9	6.1	0.31	2×3.2	3.2
2.46	15.18	12.60	10.00	8.9	6.0	0.31	2×3.2	3.2
2.23	15.18	12.60	10.00	8.9	6.0	0.30	2×3.2	3.2
2.08	15.18	12.60	10.00	8.9	5.8	0.30	2×3.2	3.2
1.93	15.18	12.60	10.00	8.9	5.8	0.28	2×3.2	3.2
1.75	15.18	12.60	10.00	8.9	5.8	0.26	2×3.2	3.3
1.41	15.18	12.60	10.00	8.9	5.6	0.23	2×3.2	3.3
1.28	15.18	12.60	10.00	9.8	5.6	0.23	2×3.2	3.3
0.98	15.18	12.60	10.00	10.0	6.1	0.23	2×3.2	3.3
0.14	15.18	12.60	10.00	10.0	6.1	0.23	2×3.2	3.3

Note: Layer thickness (LT) of bi-hydrated, mono-hydrated and dehydrated layers (2W, 1W and 0W layers, respectively) are given in Å. For hydrated layers, the amount of interlayer H₂O molecules is given per O₂₀(OH)₄. N is the mean number of layers in the coherent scattering domains, while the orientation parameter σ^* and layer thickness variability parameter σ_z are given in ° and in Å, respectively.

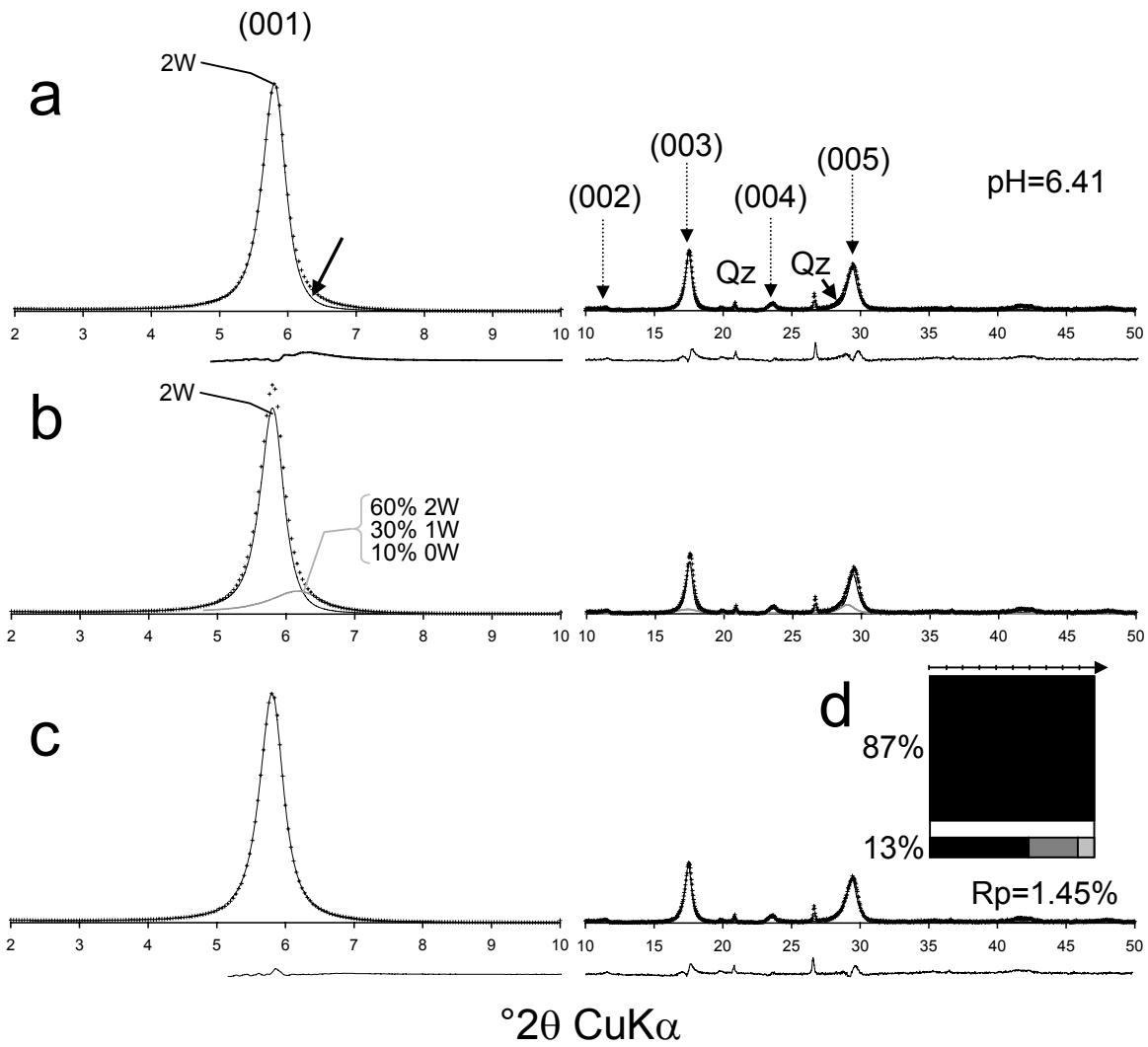
Table 3. Optimum structure parameters determined from the fitting of XRD profiles recorded for samples prepared under alkaline conditions.

pH	LT 2W	LT 1W	LT 0W	N	σ^*	σ_z	nH ₂ O 2W	nH ₂ O 1W
6.41	15.18	12.60	10.00	8.7	6.5	0.35	2×3.2	3.2
7.46	15.17	12.60	10.00	9.0	6.5	0.35	2×3.2	3.2
9.59	15.17	12.60	10.00	9.0	6.5	0.35	2×3.2	3.2
11.24	15.16	12.60	10.00	9.1	6.5	0.35	2×3.2	3.2
11.81	15.15	12.60	10.00	9.4	6.0	0.35	2×3.2	3.2
12.31	15.15	12.60	10.00	9.4	5.5	0.35	2×3.2	3.2
12.62	15.15	12.60	10.00	9.3	5.0	0.35	2×3.2	3.2

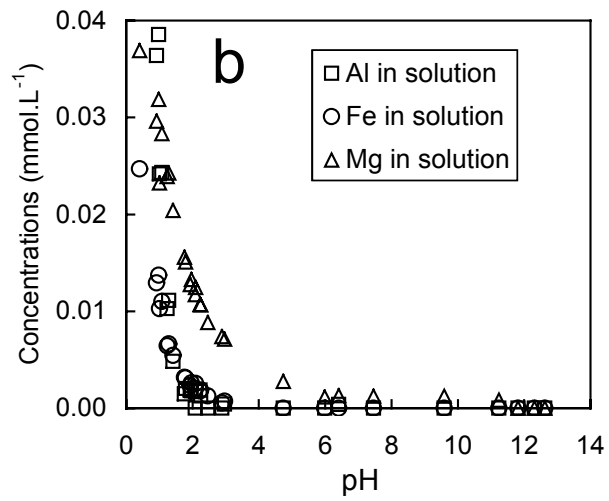
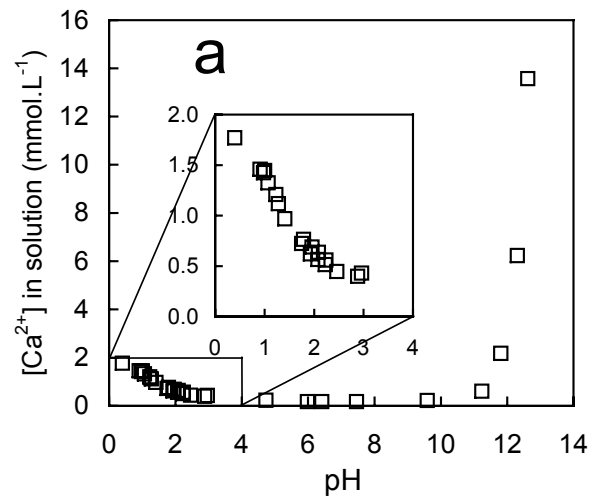
Note: Layer thickness (LT) of bi-hydrated, mono-hydrated and dehydrated layers (2W, 1W and 0W layers, respectively) are given in Å. For hydrated layers, the amount of interlayer H₂O molecules is indicated per O₂₀(OH)₄. N is the mean number of layers in the coherent scattering domains, while the orientation parameter σ^* and layer thickness variability parameter σ_z are given in ° and in Å, respectively.

Table 4. Saturation index (SI) calculated for two CSH phases as a function of pH. Ca and Si concentration conditions measured in the present study and in that of Tournassat et al. (2004a) have been used.

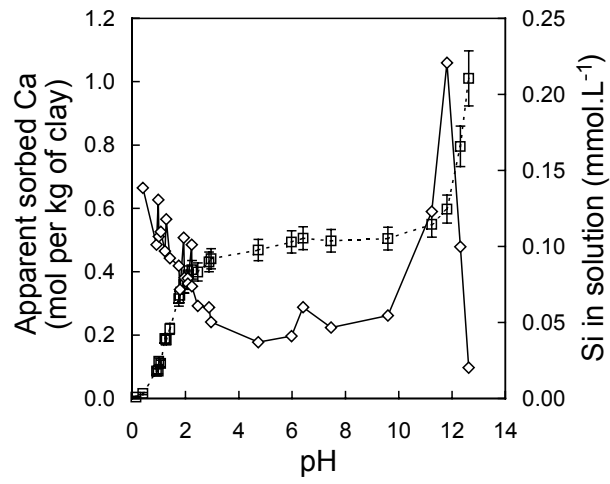
pH	[Ca] (mmol.L ⁻¹)	[Si] (mmol.L ⁻¹)	log SI CSH 0.8	log SI CSH 1.1
<i>This study</i>				
11.81	2.18	0.221	0.0	0.6
12.31	6.23	0.100	0.1	1.1
12.62	13.57	0.020	-0.4	0.9
<i>Tournassat et al. (2004a) study</i>				
11.38	5.61	0.68	0.5	1.0
11.93	4.41	0.25	0.3	1.0
10.77	50.8	0.22	0.2	0.5
11.16	50.1	0.14	0.2	0.7



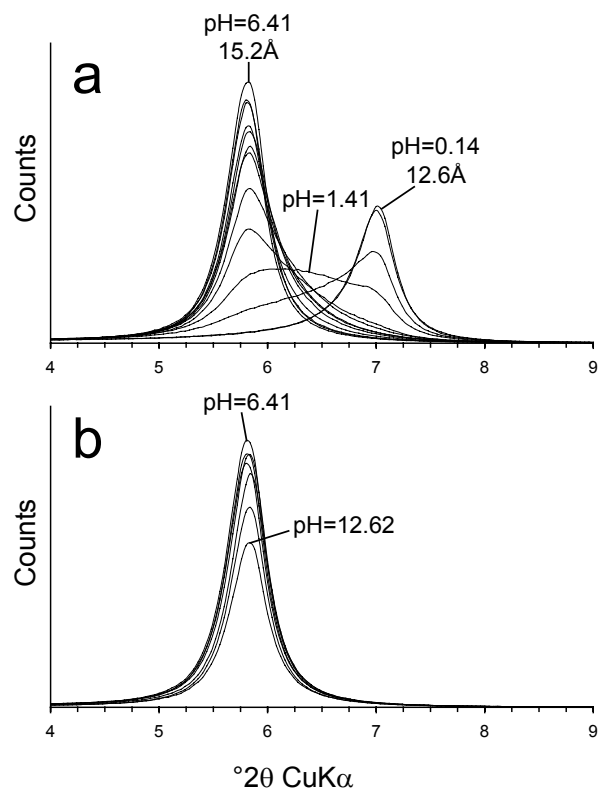
Please print in 2 column format



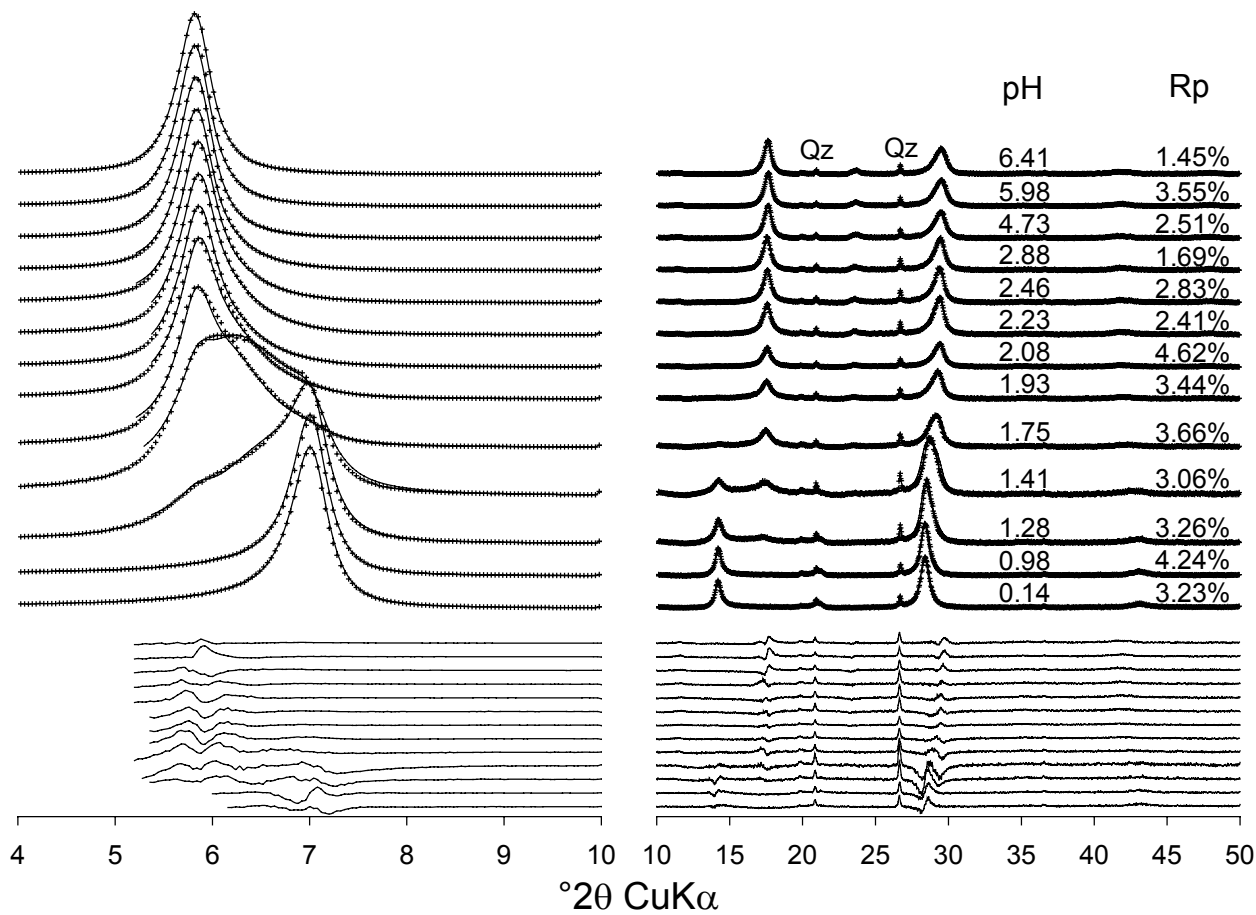
Ms#W2963 Ferrage et al. Fig. 02



Ms#W2963 Ferrage et al. Fig. 03

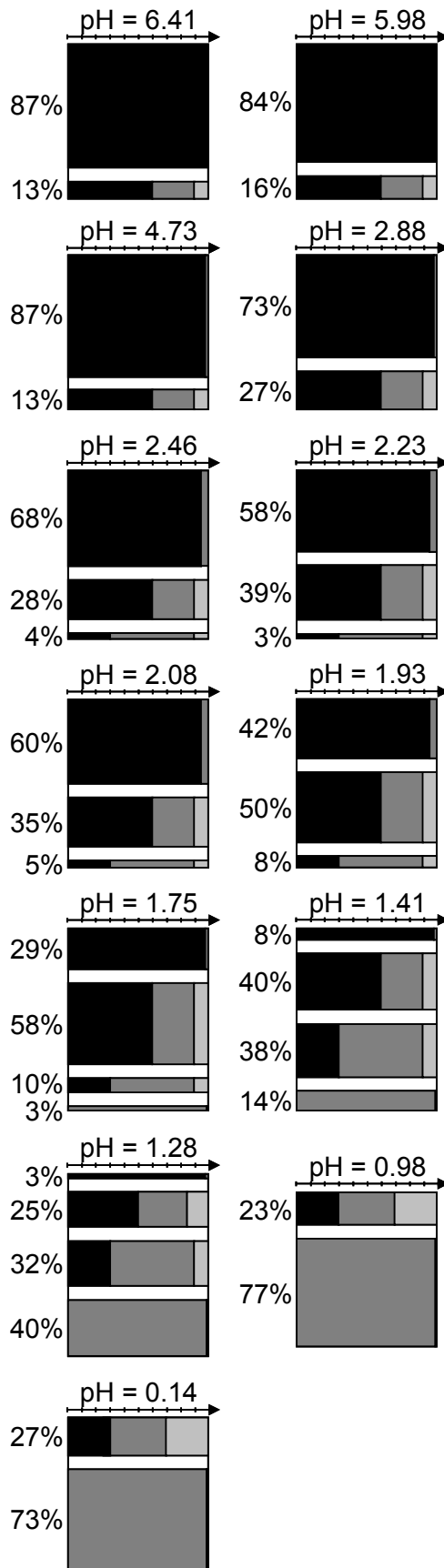


Ms#W2963 Ferrage et al. Fig. 04

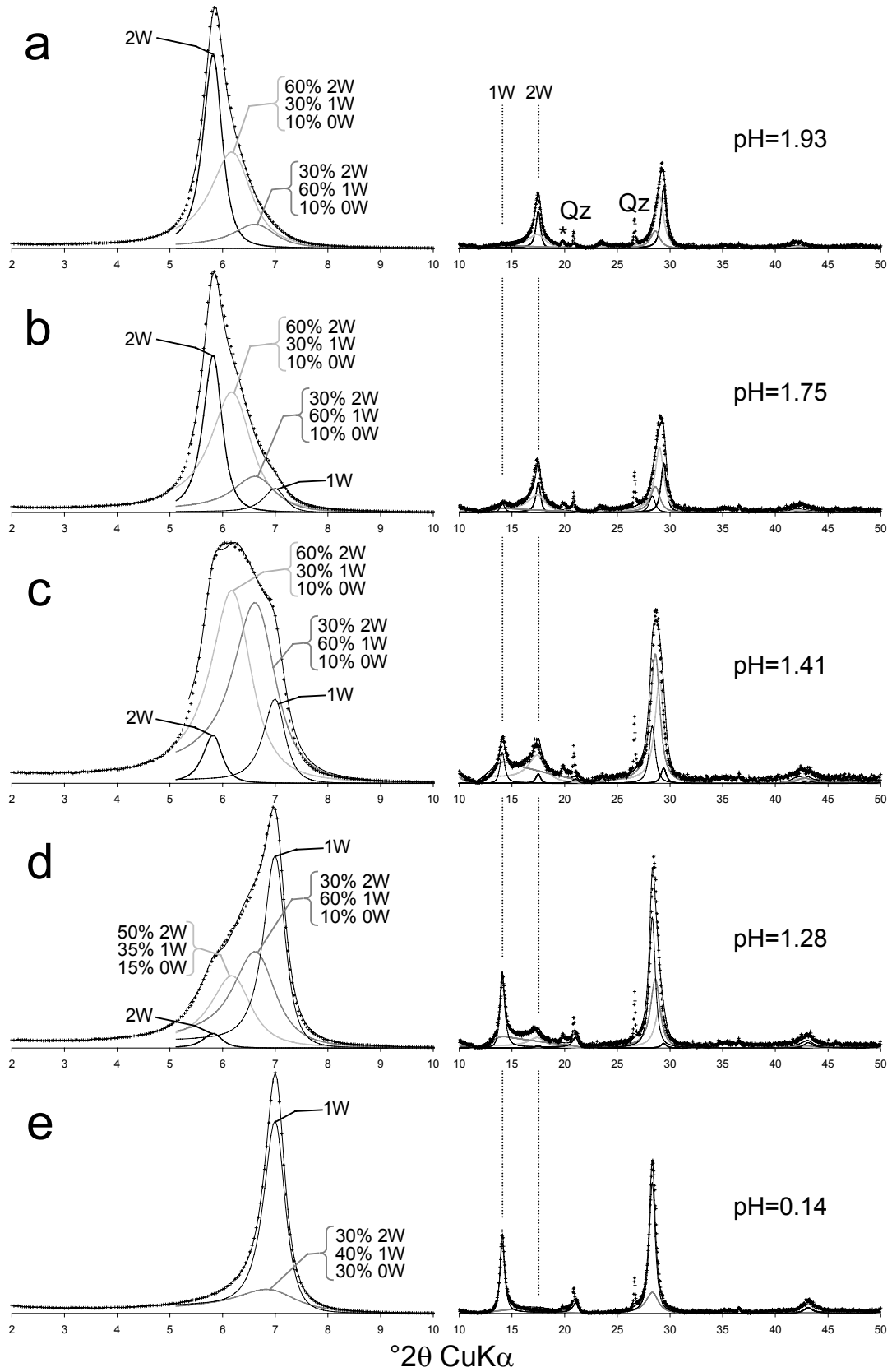


Please print in 2 column format

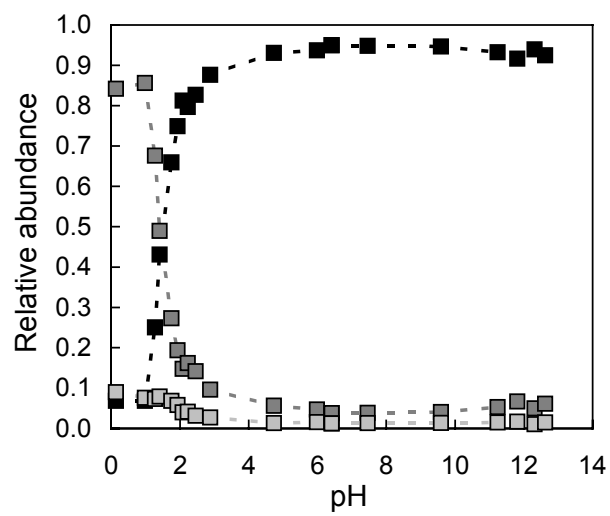
Ms#W2963 Ferrage et al. Fig. 05



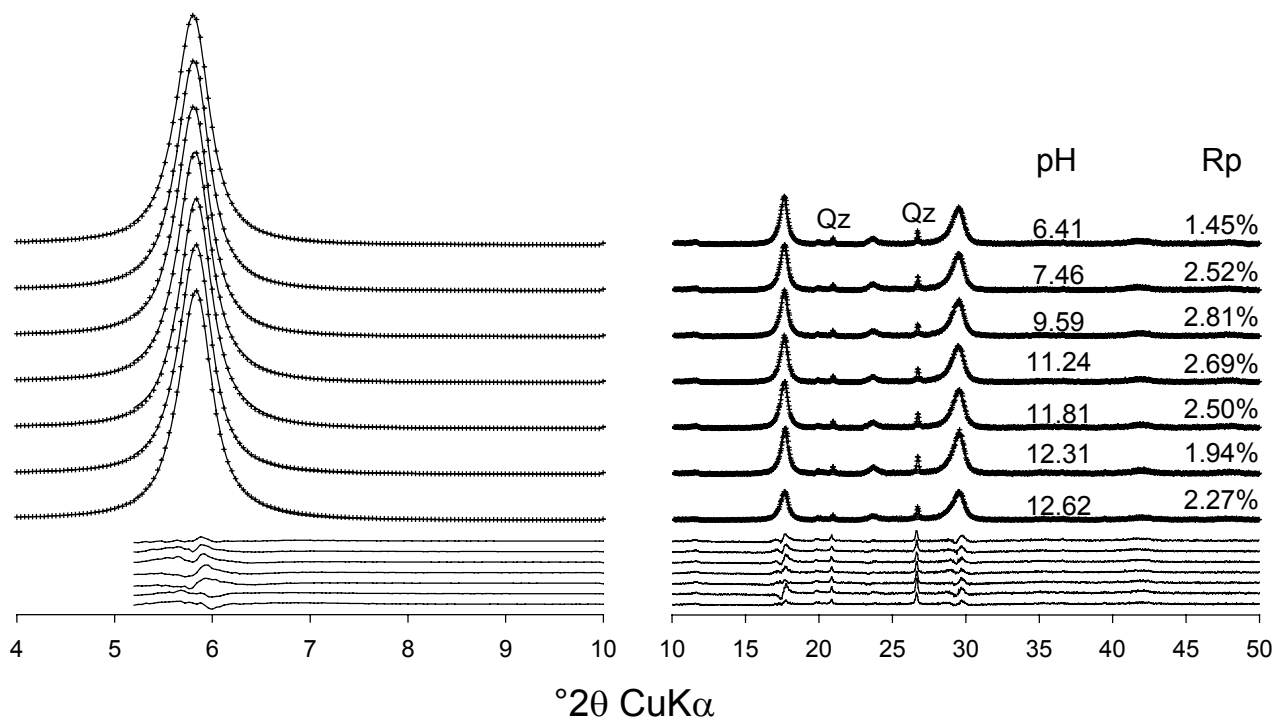
Ms#W2963 Ferrage et al. Fig. 06



Please print in 2 column format

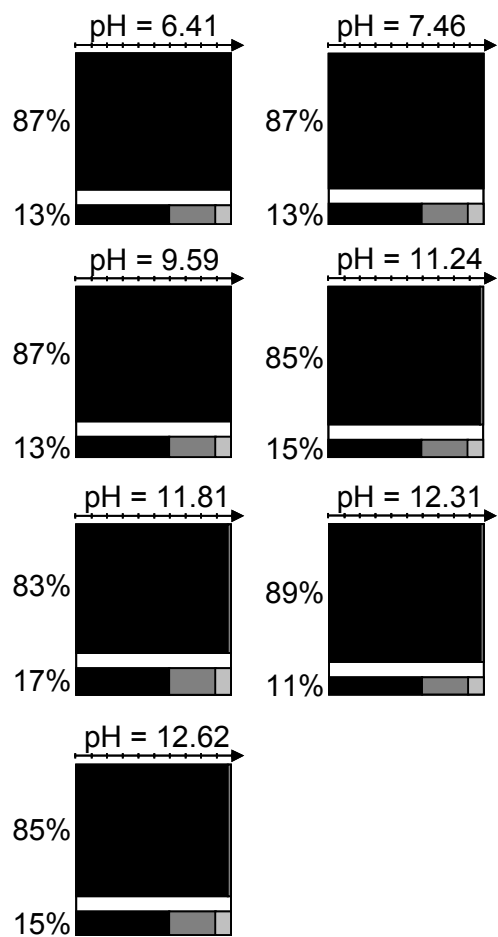


Ms#W2963 Ferrage et al. Fig. 08

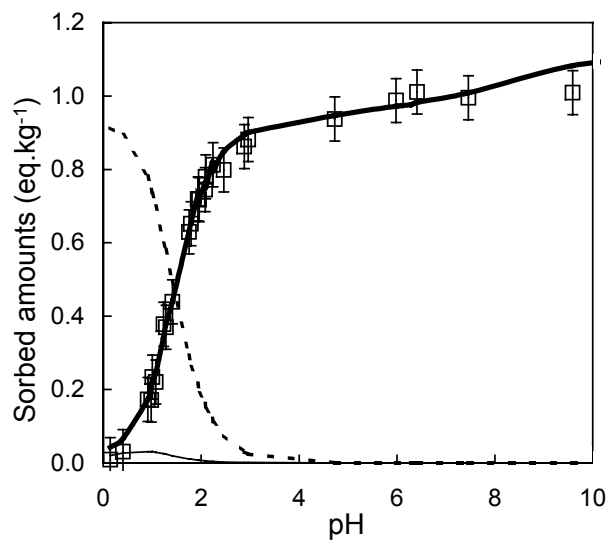


Please print in 2 column format

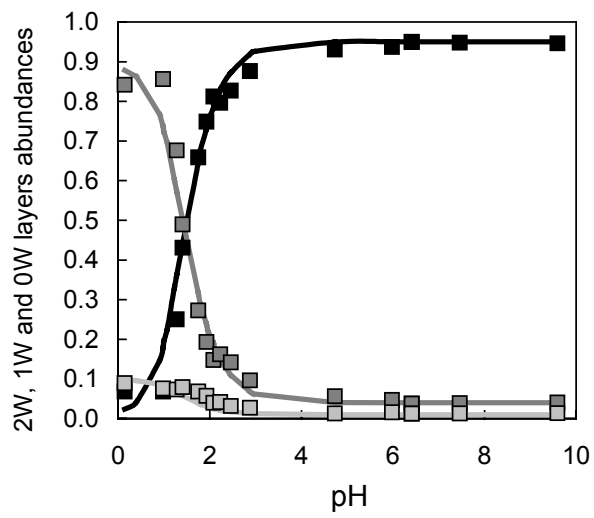
Ms#W2963 Ferrage et al. Fig. 09



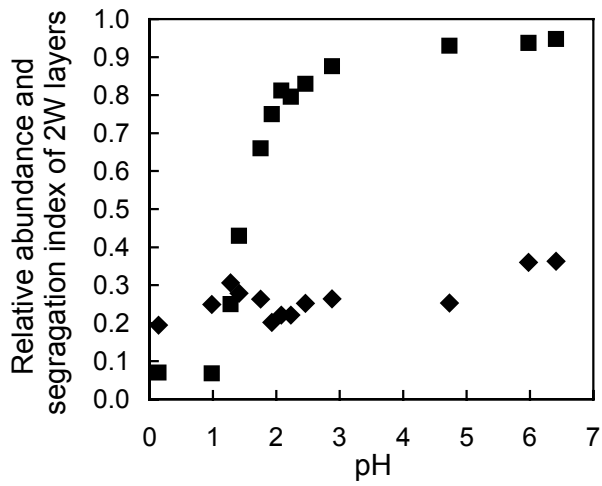
Ms#W2963 Ferrage et al. Fig. 10

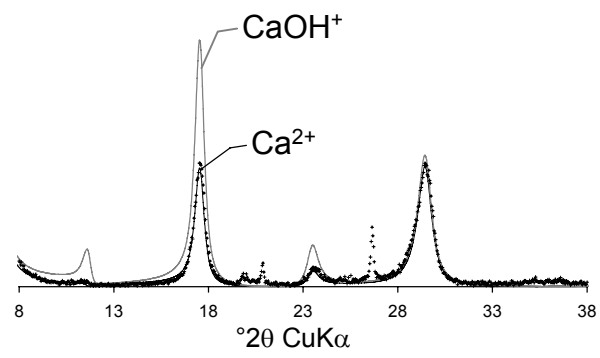


Ms#W2963 Ferrage et al. Fig. 11

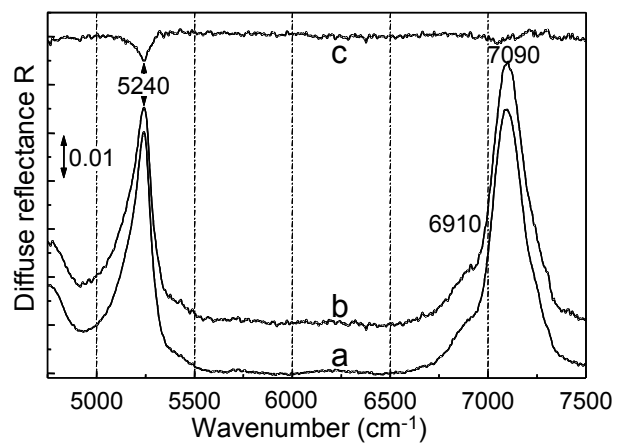


Ms#W2963 Ferrage et al. Fig. 12

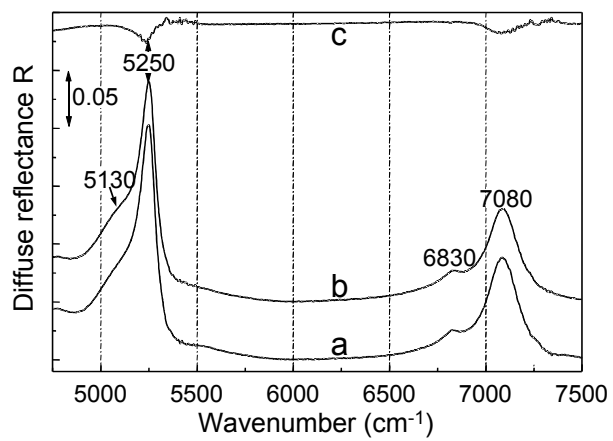




Ms#W2963 Ferrage et al. Fig. 14



Ms#W2963 Ferrage et al. Fig. 15



Ms#W2963 Ferrage et al. Fig. 16